J Mater Sci (2026) 61:15147–15171

Metals & corrosion

Rejuvenating the creep life of modified 9Cr–1Mo steel using a short-term heat treatment

Amey Parnaik[1], Manish Verma[1], Kishor Kaushal Kumar[1], Kai Chen[2], A. H. V. Pavan[3,*], and R. L. Narayan[1,*]

[1] *Department of Materials Science and Engineering, Indian Institute of Technology Delhi, Hauz Khas, New Delhi, Delhi 110016, India*
[2] *Center for Advancing Materials Performance From the Nanoscale (CAMP-Nano), State Key Laboratory for Mechanical Behavior of Materials, Xi'an Jiaotong University, Xi'an 710049, Shaanxi, China*
[3] *Metallurgy, Materials & Composites Group, Corporate R&D Division, Bharat Heavy Electricals Limited, Vikasnagar, Hyderabad 500042, India*

Received: 8 January 2026
Accepted: 1 April 2026
Published online: 20 April 2026

© The Author(s), under exclusive licence to Springer Science+Business Media, LLC, part of Springer Nature, 2026

ABSTRACT

Modified 9Cr–1Mo (P91) steel components that are used in thermal power plants undergo creep degradation during long-term service at 600 °C. This study examines the effect of a short-term rejuvenation treatment (RT), involving normalizing at 1050 °C for 2 h followed by tempering at 750 °C for 2 h, on the creep life enhancement of partially crept P91 steel at 600 °C and 135 MPa. The creep response of rejuvenated P91 steel is compared with its as-received counterpart, which is creep-tested until rupture. Results reveal that the short-term RT erases the creep history in partially crept P91 steel and enhances creep life by approximately 4 times compared to its as-received counterpart. Microstructural analysis reveals that creep leads to lath coarsening, deviates the orientation relationship (OR) between laths and prior austenite grain (PAG) from the ideal Kurdjumov–Sachs (K–S) OR, Oswald ripening of $M_{23}C_6$ precipitates, and a reduction in dislocation density, ρ. RT on the partially crept P91 leads to a complete microstructure reversal, wherein the microstructural features match well with the uncrept as-received sample subjected to the same treatment. Microstructural evolution during creep, involving the competition between dislocation climb-assisted lath coarsening and lath boundary pinning by $M_{23}C_6$ precipitate, is discussed and numerically estimated from the continuum damage model (CDM). Correlations are established between the initial lath width, lath coarsening kinetics, steady-state lath width, and creep rate. Implications of these results on extending the life of P91 components and the effectiveness of RT compared to similar rejuvenation treatments on other high-temperature alloys are discussed.

Handling Editor: Zhao Shen.

Address correspondence to E-mail: pavanahv@bhel.in; rlnarayan@iitd.ac.in

https://doi.org/10.1007/s10853-026-12714-y

Introduction

Modified 9Cr–1Mo tempered martensitic steel, also known as Grade 91 or P91 steel, is used for fabricating steam pipes in nuclear and thermal power plants as it exhibits good creep resistance in the temperature range of 600 to 650 °C [1–3]. The microstructure of P91 steel comprises prior austenite grains (PAGs) within which different variants of martensitic laths are present [4]. Moreover, it contains several $M_{23}C_6$ and MX precipitates at lath, block and PAG boundaries as well as within the intra-lath region. Before deployment in service, P91 steel components are normalized at 1040–1080 °C and then cooled in air [5]. During normalizing, martensite transforms to austenite, and the $M_{23}C_6$ and MX precipitates undergo full and partial dissolution, respectively. However, air cooling retransforms the austenite to martensite, which is hard and brittle. To alleviate the transformation-induced stresses in martensite, a tempering treatment is performed in the temperature range of 730–780 °C [5]. This leads to coarsening of laths and the precipitation of $M_{23}C_6$ and MX phases at microstructural interfaces (lath, blocks, and PAG boundaries) as well as within the intra-lath region [6–9].

Several prior studies have documented the creep behavior of tempered martensitic steels in the temperature range of 550–650 °C [7, 8, 10–13]. In these studies, it was determined that creep deformation primarily occurs in the steady-state regime and is governed by a dislocation climb-controlled mechanism, where dislocations have to climb past $M_{23}C_6$ and MX precipitates to annihilate with their opposing pairs [12, 14, 15]. In the process of dislocation annihilation, the lath subgrain boundaries migrate leading to lath coarsening, which is significantly higher than what occurs during isothermal annealing at the same temperature [12]. Excessive growth leads to microstructural instability, which in turn corresponds to the onset of tertiary creep in the alloy [7].

Following the work of some groups on performing secondary heat treatments to improve the fatigue and impact toughness of P91, we investigated the effect of a secondary short-term normalizing and tempering treatment on its creep behavior in a previous study [11]. Our results indicated that the secondary normalizing treatment followed by the short-term tempering treatment for 2 h significantly refines the lath subgrains compared to that in the as-received condition. Subsequent creep investigations revealed that the alloy that undergoes this secondary heat treatment has significantly higher creep life compared to that of its as-received counterpart. For instance, at the prescribed service conditions of 150 MPa and 600 °C, the former has sixfold higher creep life than that of the latter. Motivated by this observation, we considered the possibility of employing this heat treatment on a P91 component, which has been exposed to service, to extend its creep life significantly. If successful, this short-term heat treatment strategy can be adopted in service to improve the operational life of the component, which in turn can have enormous economic benefits. This strategy, known as *creep life rejuvenation*, draws inspiration from similar efforts made in the aerospace industry, particularly for Ni-based superalloy turbine blades in aircraft engines [16–21]. These blades, which also undergo creep at elevated-temperature service, are both costly and composed of precious constituents. In these alloys, creep life rejuvenation strategies such as heat treatment, re-coating, and hot isostatic pressing, have been successfully employed to partially recover the initial microstructure, which enhances the creep life of these components to a great extent [21].

To the best of our knowledge, this is the first study to quantify the creep rejuvenation potential of ferritic martensitic steel, which provides direct experimental and analytical evidence of creep life recovery through controlled short-term heat treatment. To determine the potency and influence of the proposed creep rejuvenation treatment for P91 steel, an as-received P91 steel sample, which has undergone creep at the prescribed service conditions for half its predicted rupture life, is subjected to the above-mentioned short-term normalizing and tempering treatment. Thereafter, this treated sample is again creep-tested in the same conditions until rupture. For reference, another as-received specimen is creep-tested up to failure without performing the rejuvenation treatment. Results reveal that the rejuvenation treatment largely restores the creep history of the tested sample and enhanced its creep life by a factor of ~ 4, which is the enhancement expected from an uncrept sample that is subjected to the same heat treatment. To understand the mechanisms that lead to this complete creep life rejuvenation, the evolution of key microstructural features of the creep-tested samples, such as lath sub-grain width, precipitates, the interstitial carbon in laths, and lath reorientation, is studied post-partial creep deformation, post-rejuvenation treatment, and post-creep rupture in significant detail. Thereafter, the lath coarsening dynamics and precipitate growth

of creep-tested samples are studied by employing the continuum damage model (CDM) developed by Xiao et al. [12]. Finally, an empirical correlation between the lath sub-grain width and steady-state creep rate is established, and a quantitative estimate of % growth in lath size in the secondary regime is obtained. Utilizing these observations, some key insights on applying the creep life rejuvenation treatment on P91 steel are provided.

Experiments

Materials

A 16-mm-thick cold-rolled plate of modified 9Cr–1Mo ferritic martensitic steel (FMS), commonly referred to as "P91" steel, is chosen in this study. The chemical composition of P91 steel, measured using optical emission spectroscopy, is presented in Table 1. The alloy is austenitized at 1050 °C for 6 h and then rapidly quenched in oil. Following this, the alloy is tempered at 750 °C for 15 h and subsequently air-cooled to room temperature. In this state, the alloy will hitherto be referred to as the as-received (AR) alloy.

Creep tests and intermediate rejuvenation treatment

Creep tests are performed with a single-lever arm type dead weight creep machine with a lever arm ratio of 20:1 equipped with a PID-controlled three-zone furnace. Cylindrical samples with gauge section length and diameter of 25 mm and 5 mm, respectively, with their longitudinal axis parallel to the rolling direction, are extracted from the AR plate for creep tests. First, a creep test is performed at 600 °C and 135 MPa. The temperature of 600 °C represents typical operating conditions for P91 steel piping in thermal power plants [13, 22], while the applied stress is intentionally higher than the usual service hoop stress in piping (~ 60–90 MPa) to accelerate creep damage within a practical laboratory timescale. From this test, the rupture time/creep lifetime, t_r, of the AR sample is determined and set as its benchmark rupture time. Next, two additional creep tests at the same temperature and stress are performed on the AR samples and interrupted after reaching $0.5t_r$. While one of these partially creep-deformed samples tested up to $0.5t_r$ is utilized for post-creep characterization, the other is subjected to a 'rejuvenation heat treatment' (RT). RT treatment involves austenitization of the partially creep-deformed AR sample at 1050 °C for 2 h, followed by air-cooling, and subsequent tempering at 750 °C for 2 h, followed by air cooling to room temperature. After this, the RT treated partially crept sample, which will hitherto be referred to as the RT sample is again creep-tested at 600 °C and 135 MPa. To understand the effect of the RT treatment on the undeformed AR sample, creep tests are also performed on AR plate that is subjected to the RT treatment. This sample will hitherto be referred to as the 'RTUD' condition. A schematic illustration of the thermal treatments on the AR, RT, and RTUD samples is shown in Fig. 1. The rationale for the choice of creep test interruption time and the RT treatment will be provided later. In a strain versus time plot, the duration of each creep stage is calculated by identifying the start of the secondary stage, where the curve becomes linear and has a constant slope, and the onset of the tertiary stage where the slope of the curve deviates from linearity and rises steeply.

Tensile tests

Three sets of tensile specimens with gauge length, width, and thickness of 18 mm, 3 mm, and 2 mm, respectively, are extracted from AR and RTUD plates. Uniaxial tensile tests are performed on three specimens in each case at 25 °C and 600 °C, at a nominal strain rate of 10^{-3} s^{-1}. To ensure precise determination of Young's modulus and plastic strain, a video extensometer is employed to measure displacement during the tensile tests.

Microstructural characterization

For metallographic analysis of AR, RT, and RTUD samples, smaller pieces are extracted and sequentially ground using emery papers ranging from coarse to fine with varying grit sizes. This is followed by the final polishing step using 0.05-μm non-crystallizing colloidal silica suspension. Subsequently, the specimens are etched using a freshly prepared Vilella's

Table 1 Chemical composition (in wt. %) of P91 steel

Element	C	Cr	Mo	Nb	Mn	Ni	V	W	Si	P	S	N	Fe
Content	0.15	8.85	1.14	0.078	0.35	0.19	0.24	0.03	0.42	0.003	0.003	0.04	Bal

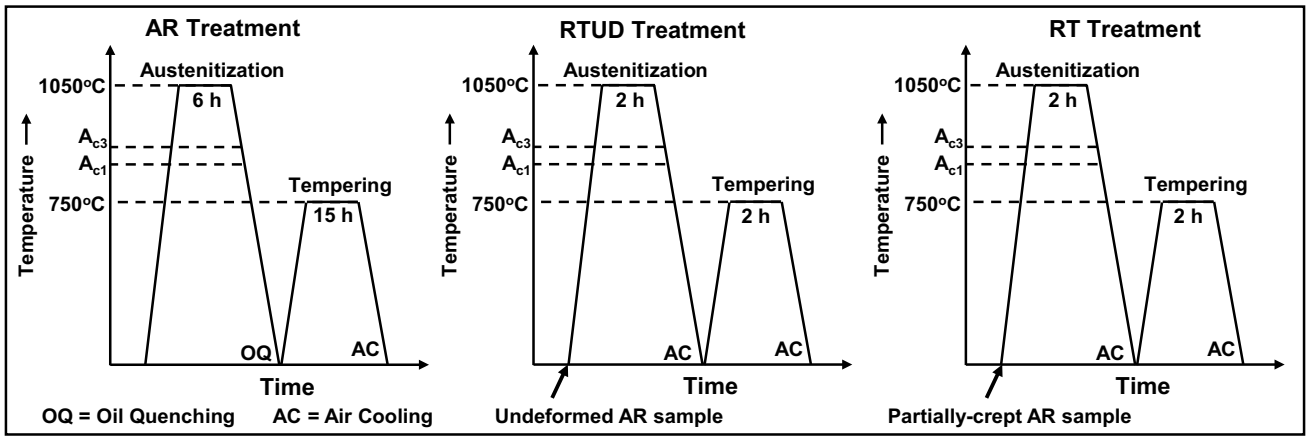


Figure 1 Schematic illustration of thermal treatments on AR, RTUD, and RT samples.

reagent consisting of 1 g picric acid, 5 mL HCl, and 100 mL ethanol. Microstructural characterization and elemental composition analysis are performed using JEOL JSM-7800F prime field emission scanning electron microscope (FESEM) operating at an accelerating voltage of 20 kV and an integrated Oxford Instruments energy-dispersive X-ray spectroscopy (EDS), respectively. Microstructural observations are carried out on undeformed samples as well as on crept samples within the uniformly deformed gauge portion, which are located ~ 20 mm away from the fracture surface. Also, the size and area fraction of the precipitates are measured by considering at least 200 precipitates and corroborated with the size distribution obtained from bright-field TEM micrographs. To understand the texture evolution before and after the rejuvenation treatment and subsequent creep tests, electron backscattered diffraction (EBSD) scans are performed on the above-mentioned FESEM, which is also equipped with an Oxford Instruments EBSD detector. The scans utilized a step size of 0.5 μm over an area of 300 × 300 μm^2. Leveraging the EBSD data, the analysis of prior austenite grains, packets, and blocks is performed using the open-source MTEX software. To generate maps at the block scale, a critical misorientation angle of 3° is selected. The evaluation process employs the two-step variant graph algorithm, which takes into account the Kurdjumov–Sachs (K–S) orientation relationship (OR) between austenite and martensite, alongside the crystallographic orientation of each variant [23]. Although alternative ORs, such as the Nishiyama–Wassermann (N-W) and Greninger–Trojano (G-T), exhibit a slight misorientation angle of about 2.5°, they are expected to induce only minor variations in the microstructural response [4, 24]. The algorithm used for analyzing ORs in this study is presented in detail by Niessen et al. [23, 25] in their recent publications.

For a comprehensive analysis of sub-grains, dislocation density, their interactions with precipitates, and precipitate characterization, the study employs the JEOL JEM-ARM200F NEOARM high-resolution transmission electron microscopy (HRTEM), equipped with a cold field emission gun (FEG) operating at 200 kV. These foils are subjected to electrolytic thinning in a solution of 10% perchloric acid and 90% ethanol, followed by ion milling using the PIPS II equipment, before being transferred to the HRTEM for examination. Precipitate size, area fraction, interparticle spacing, and lath/sub-grain width were measured from at least two to three independent TEM foils per condition, with 8–10 representative fields of view analyzed in total for each case. All measurements were taken from the gauge section at least 20 mm away from the fracture surface to avoid the influence of localized tertiary damage or necking. No significant microstructural gradients were observed within TEM foils extracted from these regions. Particle size and area fraction were obtained by considering at least 200 particles in each case. Note that particle sizes were determined using identical magnification, thresholding, and particle selection criteria across all conditions.

Results

Microstructure of uncrept AR and RTUD samples

Figures 2 and S1 show the microstructures of the uncrept AR and RTUD samples. The size of the prior austenitic grains (PAGs) in uncrept AR and RTUD samples is 21 ± 4 and 30 ± 3 μm, respectively. These PAGs are subdivided into several small units, each exhibiting a set of crystallographically related variants formed during martensitic transformation [4, 24]. These crystallographically related variants are organized into five levels of hierarchy, which are individual martensitic laths (see Figs. 2a–c, S1a–c), sub-blocks formed by adjacent laths of the same variant, blocks composed of sub-blocks of two variants misoriented by a small angle (see Figs. 2d, f, S1d, f), packets containing blocks with nearly identical $\{111\}_\gamma//\{011\}_\alpha$ orientations (see Figs. 2g, S1g), and PAGs consisting of interpenetrating packets (see Figs. 2h, S1h).

In both uncrept AR and RTUD samples, martensitic laths have an OR with parent austenite grain that deviates slightly from K–S, G–T, and N–W ORs [26]. However, most laths in both samples can be characterized as having a near K–S OR, as is observed in Figs. S2 and S3. In the K–S orientation, laths in a packet share the same plane parallel relationship between parent (austenite) and child (martensite) closed-packed planes, resulting in four crystallographically distinct packets,

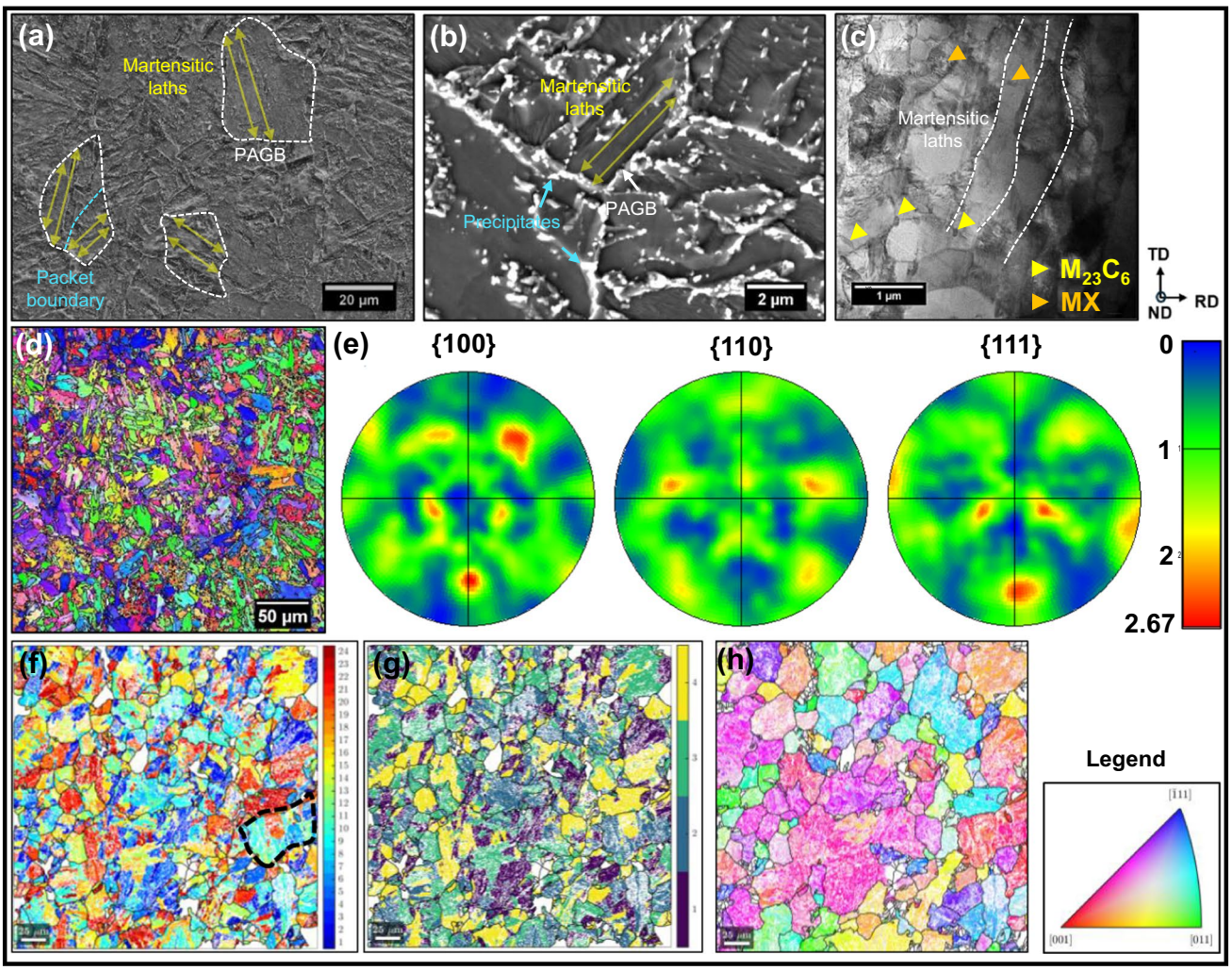


Figure 2 **a** Low- and **b** high-magnification SEM images, **c** bright-field TEM image, **d** inverse pole figure (IPF) map, **e** pole figures, **f** 24 variants in martensitic blocks observed according to K–S OR, **g** corresponding packets, **h** reconstructed parent austenite grains of uncrept AR sample.

within an austenite grain, which are represented by 4 different colors, as shown in Figs. 2g and S1g. Figure S4 further illustrates the OR between 24 K–S variants as listed in Table S1.

In Figs. 2a and S1a, translucent yellow arrows denote the positioning of the martensitic lath within packets and PAGBs in uncrept AR and RTUD samples, respectively. The corresponding high-magnification secondary electron (SE) image of this region, shown in Figs. 2b and S1b, reveals a high-density of nano-sized precipitates in the two samples. These precipitates are located at PAGBs, packet boundaries, block boundaries, and lath or sub-grain boundaries as well as within the intra-lath (or within the sub-grains) regions. TEM images of the uncrept AR and RTUD samples are shown in Figs. 2c and S1c, respectively. From these images, the average lath or sub-grain width, L, is measured and listed in Table 2. In the uncrept AR sample (see Fig. 2c), several martensitic laths and equiaxed sub-grains with L of 676 ± 54 nm are observed. In comparison, the uncrept RTUD sample has a finer L of 552 ± 35 nm. In this context, lath and sub-grains are distinguished based on their aspect ratios, with the former being elongated (length/width > 3) in one direction and the latter being nearly equiaxed (length/width ≤ 3). However, owing to their otherwise similar origins and characteristics, they will hitherto be collectively referred to as 'lath sub-grains'.

Additionally, the lath sub-grain boundaries contain $M_{23}C_6$-type precipitates, whereas the MX (X: C or N)-type precipitates are found within the lath sub-grains [11]. The average sizes of the two precipitates, d_{M23C6} and d_{MX}, area fractions, A_{M23C6} and A_{MX}, and their interparticle spacings, δ_{M23C6} and δ_{MX}, in the uncrept AR and RTUD are measured and listed in Table 2. The interparticle spacing (δ) is calculated using the relation $\delta = \left(\frac{d}{2}\right)\left(\frac{4\pi}{3A}\right)^{1/3}$ and the standard deviation was estimated by recalculating δ using the upper and lower bounds of precipitate sizes. In the uncrept AR sample, d_{M23C6} and d_{MX} are 164 ± 18 nm and 30 ± 5 nm, respectively whereas in the uncrept RTUD sample, they are 122 ± 8 nm and 22 ± 4 nm, respectively. Similarly, δ_{M23C6} and δ_{MX} are 295 ± 65 nm and 141 ± 47 nm, respectively, in uncrept AR sample, those in the uncrept RTUD sample are 267 ± 35 nm and 104 ± 38 nm, respectively, which are slightly smaller. However, while in uncrept AR and RTUD samples, A_{M23C6} is 9% and 5%, respectively, and A_{MX} is 0.5% in both samples (see Table 2). The dislocation densities, ρ, of the uncrept AR and RTUD samples are measured from multiple TEM images and XRD analysis and listed in Table 2. ρ in the uncrept AR and RTUD samples is ~ $4.05 \times 10^{14}/m^2$ and ~ $5.53 \times 10^{14}/m^2$, respectively, which is similar to that observed in our previous study [11]. Figure S5 displays an HRTEM image of the laths in the uncrept AR sample. The corresponding inverse fast Fourier transform (IFFT) patterns for the (112) and (211) planes are also shown. Using the equation for the body-centered tetragonal (BCT) structure

$$\frac{1}{\lambda^2} = \frac{h^2 + k^2}{a^2} + \frac{l^2}{c^2}, \quad (1)$$

where λ represents the interplanar spacing, a and c are the lattice parameters, and the c/a ratios of the uncrept AR and RTUD samples are calculated and listed in Table 2. The lattice parameters for the tempered martensitic phase in uncrept AR sample are $a = 2.870$ Å and $c = 2.874$ Å, which corresponds to the c/a ratio of 1.0014. In comparison, the uncrept RTUD sample has a c/a ratio of 1.0064, indicating that it is comparatively more distorted. This is also validated by high-resolution X-ray diffraction measurements and is described in our previous study [11].

Table 2 Microstructural features in uncrept, partially crept, and creep-ruptured P91 steel samples

Condition	$M_{23}C_6$			MX			L (nm)	ρ (m^{-2})	c/a ratio	MUD
	d_{M23C6} (nm)	A_{M23C6} (%)	δ_{M23C6} (nm)	d_{MX} (nm)	A_{MX} (%)	δ_{MX} (nm)				
Uncrept AR	164 ± 18	9	295 ± 65	30 ± 5	0.5	141 ± 47	676 ± 54	4.05×10^{14}	1.0014	2.67
Uncrept RTUD	122 ± 8	5	267 ± 35	22 ± 4	0.5	104 ± 38	552 ± 35	5.53×10^{14}	1.0064	2.55
Partially crept AR	188 ± 13	9	338 ± 47	32 ± 3	0.5	151 ± 28	857 ± 64	1.24×10^{14}	1.0000	8.28
Uncrept RT	114 ± 15	5	250 ± 66	24 ± 2	0.5	113 ± 19	448 ± 41	6.56×10^{14}	1.0065	2.30
Creep-ruptured AR	234 ± 21	9	421 ± 76	32 ± 4	0.5	151 ± 38	959 ± 85	0.95×10^{14}	1.0000	11.50
Creep-ruptured RT	170 ± 14	9	306 ± 50	25 ± 4	0.7	76 ± 34	998 ± 78	0.98×10^{14}	1.0000	2.40

The inverse pole figure (IPF) maps of uncrept AR and RTUD samples are shown in Figs. 2d and S1d, respectively. EBSD scanning is performed on the rolling direction–transverse direction (RD-TD) plane. IPF maps reveal that blocks have a diffuse orientation throughout the scanned area. The width of blocks is calculated by first identifying the trace of the habit plane for each block. Subsequently, a perpendicular line to the habit plane is plotted to measure the width of the block, as illustrated in Fig. S6a, for one PAG. The average block widths of uncrept AR and RTUD samples are ~ 1.1 ± 0.1 and 1.5 ± 0.2 μm, respectively, and the log-normal distribution best describes the scatter in the widths (see Fig. S6b). The diffused texture of blocks in both samples is further confirmed by the {100}, {110}, and {111} pole figures shown in Figs. 2e and S1e. Across all the pole figures, for the AR and RTUD samples, the highest multiple of uniform pole density (MUD) is measured and listed in Table 2. MUDs of the two samples are 2.67 and 2.55, respectively, which confirms the randomness of their textures. The ideal and measured K–S crystallographic OR between parent austenite and child martensite phase for a PAG with the highest Schmid factor for {110} < 111 > slip system are shown in Fig. S7 for both uncrept AR and RTUD samples. The PAGs of uncrept AR and RTUD samples that have the highest Schmid factor are outlined by a black dashed line in Figs. 2f and S1f, respectively. In both samples, the measured OR between parent austenite and child martensite phase only marginally deviates from the ideal K–S OR. Overall, it is evident that the RT treatment employed on the uncrept AR alloy slightly increases the PAG size, decreases d_{M23C6} and d_{MX} precipitates, decreases L, but increases its distortion and ρ marginally. These results match well with those from our previous study on the effect of the short-term re-austenizing and re-tempering treatment on the uncrept AR sample [25].

Tensile properties of uncrept AR and RTUD samples

Figure 3a shows the engineering stress (S) versus engineering strain (e) plot for uncrept AR and RTUD samples at 25 °C and 600 °C. At 25 °C, the yield strength (YS), ultimate tensile strength (UTS), and strain to failure (% elongation) of the uncrept AR sample are 509 ± 12 MPa, 644 ± 21 MPa, and 18 ± 2%, respectively. Alternately, the YS, UTS, and % elongation of the uncrept RTUD sample are 570 ± 16 MPa, 708 ± 23 MPa, and 15 ± 1%, respectively. At 600 °C, the YS and UTS of the uncrept AR sample dramatically drop to ~ 302 ± 8 MPa and 405 ± 12 MPa, respectively. Similarly, in the uncrept RTUD sample, YS and UTS drop to 354 ± 7 MPa and 450 ± 9 MPa, respectively. However, there is not much change in the % elongation of uncrept AR and RTUD samples, which are ~ 15 ± 1 and 14 ± 1, respectively. This indicates that the RT treatment enhances the strength of the uncrept AR samples only by 10–15% and has no influence on ductility.

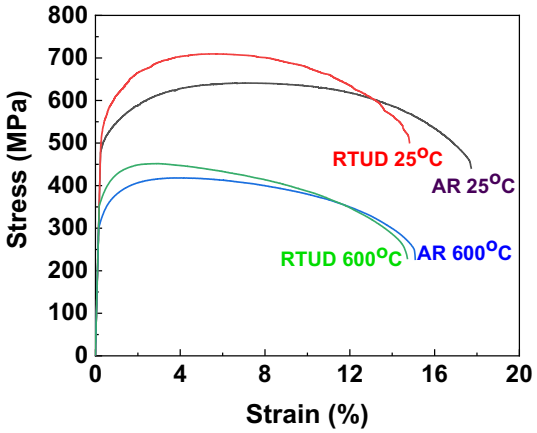


Figure 3 Tensile stress–strain responses of AR and RTUD P91 steel at 25 °C and 600 °C temperature.

Creep testing

Figure 4a shows the creep strain, ε, versus time, t, plots, for the AR and RT samples at 600 °C and 135 MPa. The response of interrupted creep test on the AR sample is also included in the plot for reference. For clarity, the AR sample that is interrupted during creep will henceforth be referred to as the partially crept AR sample to distinguish it from the creep-ruptured AR sample. Creep deformation in creep-ruptured AR and RT samples follows a pattern of small instantaneous strain upon loading, followed by a brief primary creep stage, a distinct secondary stage, and an extended tertiary creep stage. The rupture time, t_r, and durations of the primary, secondary, and tertiary regimes of creep of both samples are listed in Table 3. The % of life spent in each creep regime is included within brackets in the columns listing the durations of primary, secondary, and tertiary creep. t_r for the creep-ruptured AR sample is 992 h, out of which, 86 h is the short primary creep regime, 449 h is the

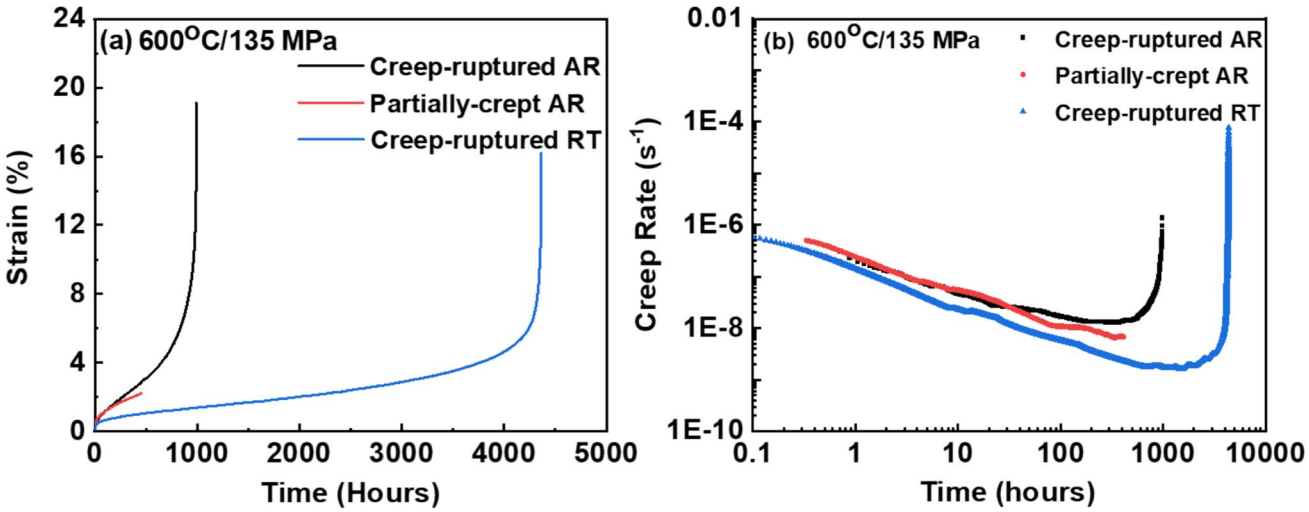


Figure 4 **a** Creep strain versus time plot of creep-ruptured AR, partially crept AR, and creep-ruptured RT samples; **b** Temporal evolution of creep rate of creep-ruptured AR and partially crept and creep-ruptured RT samples.

steady-state regime, and 443 h is the tertiary regime. Note that the onset of tertiary creep occurs at ~ 56% of the total creep life. With this consideration, the interrupted creep test is performed only for 496 h, which corresponds to a duration of $0.5t_r$ for the creep-ruptured AR sample. This essentially implies that when the test is interrupted, the partially crept AR sample is in the steady-state creep deformation stage. In contrast, t_r of the creep-ruptured RT sample is 4357 h, which is ~ 4.4 times higher than that of the creep-ruptured AR sample. Moreover, the primary, secondary, and tertiary creep regimes of the creep-ruptured RT sample are 2, 6, and 4 times higher than those of the creep-ruptured AR sample. It is also observed that, unlike the creep-ruptured AR sample, the primary creep regime of the creep-ruptured RT sample is only 3.3% of the total creep life, whereas that of the steady-state creep regime is 63%. The observed short-lived primary stage and prolonged tertiary stage is expected for creep tests performed at temperatures higher than the homologous temperature exceeding 0.4 in P91 steels [13]. Note that, according to the NIMS creep database for Grade 91 steel [27], the scatter observed in creep rupture life at any given stress and temperature typically corresponds to − 50 to + 100% of the mean creep life. This implies an expected scatter of roughly 0.5 to 2 times the mean creep life under comparable conditions. Even considering this conservative scatter envelope, the present 4.4 times increase in rupture life in RT sample substantially exceeds the upper bound of expected variability. This clearly indicates that the observed enhancement in creep performance cannot be attributed to statistical scatter.

Figure 4b illustrates the evolution of creep rate for the creep-ruptured AR and RT samples with time. The data for the partially crept AR sample, which was interrupted at $0.5t_r$, is also included for reference in the same plot. In all samples, the creep rate gradually decreases to a minimum and then dramatically increases until failure occurs. The final stage of increasing creep rate is not observed for the partially crept AR sample as its testing is interrupted in the secondary creep regime. The minimum creep rate ($\dot{\varepsilon}_{min}$) of the creep-ruptured AR and RT samples is listed in Table 3. $\dot{\varepsilon}_{min}$ of the creep-ruptured AR sample and the partially crept AR sample is ~ 1.28×10^{-8} s^{-1} and ~ 0.79×10^{-8} s^{-1}, respectively. In contrast, $\dot{\varepsilon}_{min}$ of the creep-ruptured RT sample is ~ 1.75×10^{-9} s^{-1}, which is one order of magnitude lower

Table 3 Creep data of AR and RT P91 steel

Condition	T (°C)	σ_R (MPa)	Primary creep life (h)	Secondary creep life (h)	Tertiary creep life (h)	t_r (h)	$\dot{\varepsilon}_{min}$ (s^{-1})
Creep-ruptured AR	600	135	86 (8.67%)	449 (45.26%)	443 (44.66%)	992	1.28×10^{-8}
Creep-ruptured RT	600	135	160 (3.67%)	2742 (62.93%)	1452 (33.33%)	4357	1.75×10^{-9}

than that of creep-ruptured AR and partially crept AR samples.

To compare the creep rupture lives of the samples, the Larson–Miller parameter (LMP) approach is adopted. LMP for each rupture stress is calculated from [5, 28]

$$LMP = T\left[\log\left(t_r\right) + C\right] \quad (2)$$

where T represents the creep test temperature in Kelvin (K), t_r is the rupture time in hours (h), and $C = 32$ is the material constant commonly used for P91 steel [29]. On obtaining the LMP of alloys at different stresses, provided the microstructure is stable, the long-term creep rupture life of alloys can be predicted from extrapolation [29, 30]. A plot of the rupture stress versus LMP for the creep-ruptured AR sample is displayed in Fig. 5. The data for creep-ruptured RTUD sample, which was tested in our previous study [11], are included in the same plot as a reference. Note that the LMP of the creep-ruptured AR sample for all stresses is lower than that of the RTUD sample. Therefore, from Eq. 2, it is evident that for the temperature range of 550–650 °C, the t_r of the RTUD sample is higher than that of the creep-ruptured AR sample. The data points corresponding to the creep test performed at 135 MPa and 600 °C for the creep-ruptured AR, partially crept AR, and creep-ruptured RT samples are superimposed and highlighted in the plot. Interestingly, at the rupture stress of 135 MPa, the LMP of the creep-ruptured RT sample coincides with that of the creep-ruptured RTUD sample. This implies that the RT treatment on the partially crept AR sample leads to creep resistance that is equivalent to the creep resistance of the RTUD sample, which in turn implies that RT treatment erases the creep deformation history of the P91 steel for even up to 50% of its rupture life. Note that the creep performance of RT and RTUD conditions is comprehensively compared with the NIMS (Japan) creep database and with some other literature, including detailed documentation of the corresponding heat treatment parameters, as shown in Table S3 in SI. This comparison demonstrated that the short-term heat treatment employed in our study provided superior creep performance compared to the reported values in the literature.

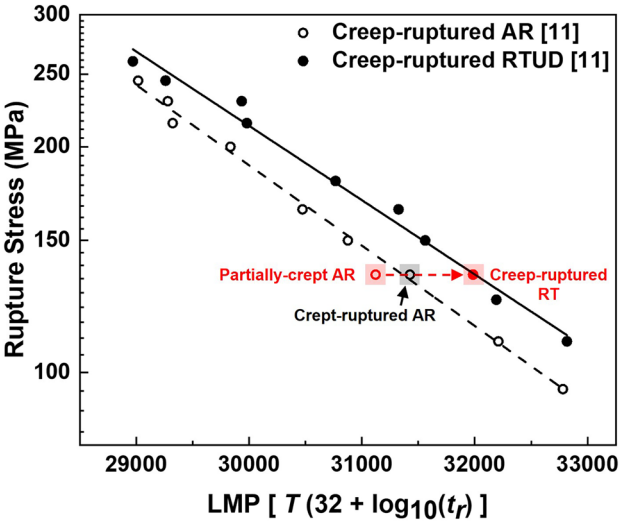


Figure 5 Rupture stress versus Larson–Miller parameter (LMP) plot for creep-ruptured AR and RTUD samples, for stresses in the range of 90 to 260 MPa at temperatures of 550 °C, 600 °C, and 650 °C. Additional data points are taken from ref. [11]. The LMP values calculated at 600 °C and a stress of 135 MPa for both creep-ruptured AR and RT samples are superimposed for comparison.

Microstructure of partially crept AR sample and uncrept RT sample

Figure 6a, b shows the microstructures of the partially crept AR sample and uncrept RT sample. Higher magnification image of the partially crept AR sample reveals (see Fig. 6c) the presence of $M_{23}C_6$ precipitates at the lath sub-grain boundaries.

Figure 7a–c, e–h shows the bright-field TEM images of the partially crept AR and uncrept RT samples, respectively. L, A_{M23C6}, A_{MX}, d_{M23C6}, d_{MX}, and their δ_{M23C6} and δ_{MX} in them are listed in Table 2. A_{M23C6} in the partially crept AR sample is ~ 9%, which is similar to that of the uncrept AR sample (see Table 2). However, d_{M23C6} and d_{MX} in the partially crept AR sample are 188 ± 13 nm and 32 ± 3 nm, respectively. In the uncrept AR sample, d_{M23C6} is 15% lower than that in the partially crept AR sample (see Fig. 7 and Table 2). Similarly, the δ_{M23C6} in the partially crept AR sample is 338 ± 47 nm, which is 15% higher than that in the uncrept AR sample.

L in this sample is 857 ± 64 nm, which is 27% larger than that of the uncrept AR sample (see Table 2). Within the lath sub-grains, several MX carbonitrides (indicated by orange arrows), $M_{23}C_6$ precipitates (indicated by yellow arrows), and Fe_2Mo-type Laves phases (indicated by blue arrows) are observed, as shown in Fig. 7b. A_{MX}, d_{MX}, and δ_{MX} is 0.5%, 32 ± 3 nm, and 151 ± 28 nm, respectively, which is similar to that of the uncrept AR sample. This indicates that the MX precipitates in the partially crept AR sample are unaffected

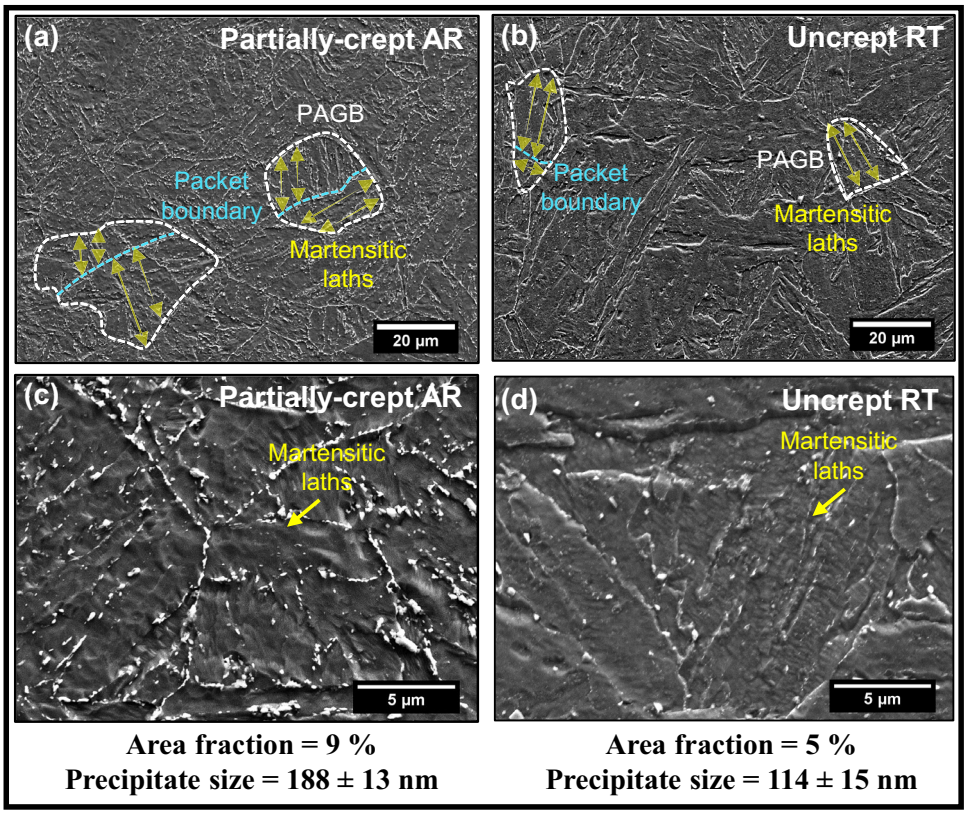


Figure 6 Microstructures of **a** and **c** partially crept AR sample, **b** and **d** uncrept RT sample.

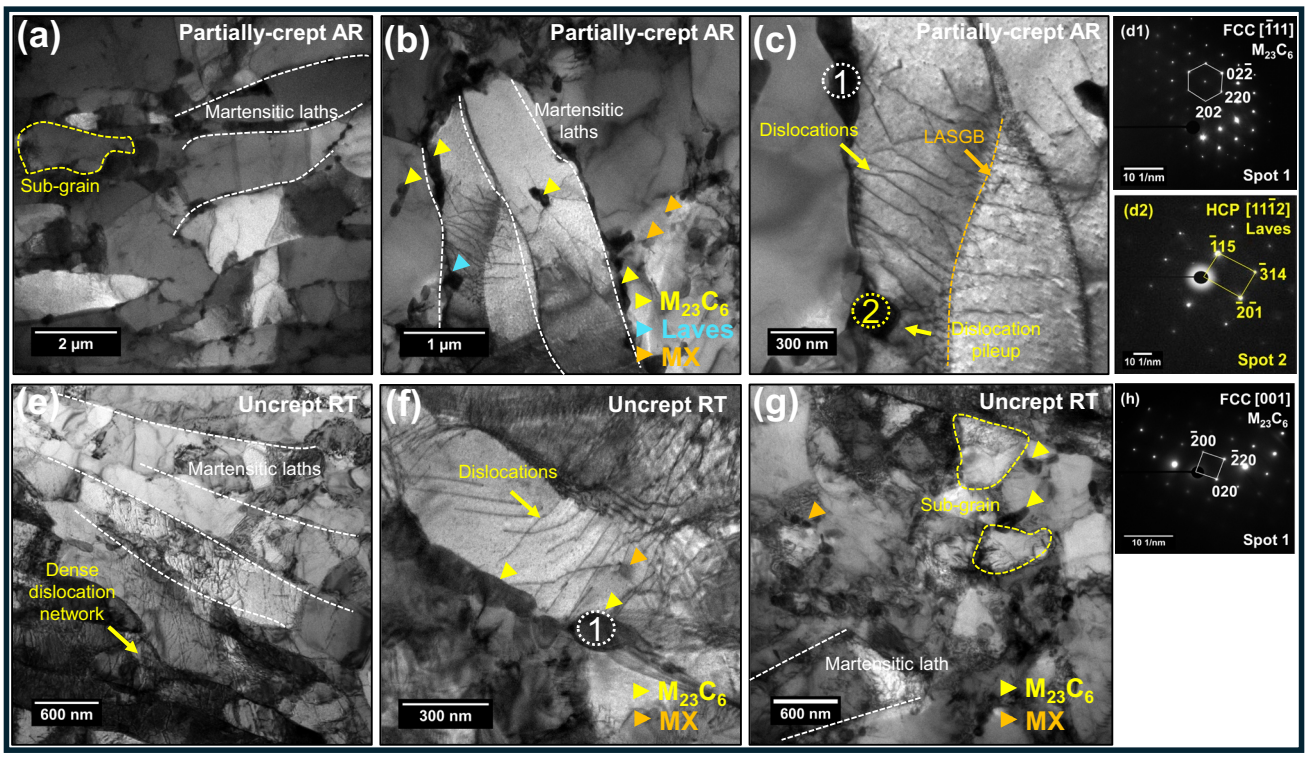


Figure 7 **a**–**c** Bright-field TEM images of the partially crept AR sample and (d1) and (d2) SAED patterns from spots 1 and 2 labeled in **c**. Bright-field TEM images of **e**–**g** uncrept RT sample and **h** SAED patterns from spot 1 labeled in **f**.

by creep. The selected area electron diffraction (SAED) patterns of these precipitates, shown in Fig. 7d1, d2, indicate that $M_{23}C_6$ precipitates have an FCC structure, whereas Laves phases have the HCP structure. The presence of Laves phases in the partially crept AR sample is further confirmed by EDS maps, shown in Fig. S9, which reveals that Mo and Si have segregated adjacent to Cr-rich $M_{23}C_6$ carbides present at the sub-grain boundaries. Isik et al. [31, 32] reported that Laves phase nucleation begins with the segregation of Mo and Si at lath sub-grain boundaries in the vicinity of $M_{23}C_6$ carbides. They suggested that with increasing time, rod-shaped Laves phases evolve by consuming $M_{23}C_6$ carbides. Furthermore, as can be seen in Fig. 7c, several dislocations pileup at the lath sub-grain boundary, near the $M_{23}C_6$ precipitates. From the TEM images, ρ and c/a ratio of the lath sub-grains are determined and listed in Table 2. Note that ρ in the partially crept AR sample is ~ 1.25×10^{14} m^{-2} and the c/a ratio of the lath sub-grain is 1. Note that SEM and TEM examination of interrupted AR sample did not reveal any creep cavities, indicating that permanent damage associated with the tertiary creep stage had not yet initiated at 0.5 t_r.

In contrast, the same microstructural features in the uncrept RT sample, shown in Fig. 7e–g and listed in Table 2, are significantly different than that of the partially crept AR sample (see Fig. 7a–d). The specific differences are as follows. First, in the uncrept RT sample, d_{M23C6} and A_{M23C6} precipitates are 114 ± 15 nm and 5%, respectively, which are both lower than that in the partially crept AR sample (see Table 2). Additionally, d_{MX} and A_{MX} are 24 ± 2 nm and 0.5%, respectively, which are finer compared to the partially crept AR sample. Second, L in the former is only 448 ± 41 nm, which is 48% lower than that of the latter (see Fig. 7e and Table 2). Third, the $M_{23}C_6$ and MX carbonitrides, located along the lath sub-grain boundaries and within the lath sub-grain interior, respectively, have much lower δ_{M23C6} and δ_{MX} of 250 ± 66 nm and 113 ± 19 nm, respectively, in the uncrept RT sample. Fourth, Laves phases are absent near the lath sub-grain boundaries. Fifth, EDS maps shown in Fig. S9b confirm that Mo and Si are uniformly distributed in the matrix. Finally, the c/a ratio and ρ are 1.0065 and 6.56×10^{14} m^{-2}, which are calculated from the TEM images of the lath sub-grains in the uncrept RT sample (see Fig. S8 and Table 2). These observations indicate that the RT treatment refines the lath sub-grains and also dissolves the Laves phases that form in the partially crept AR sample. The higher c/a ratio and ρ of the uncrept RT sample compared to the partially crept AR sample also indicate that it is significantly more distorted. Moreover, the RT heat treatment refines MX and $M_{23}C_6$ and reduces the spacing between them.

Next, the orientation of sub-grain boundaries and evolution of texture of these samples are analyzed. Figure 8a, e shows the IPF maps of the partially crept AR sample and uncrept RT sample, respectively. The corresponding block structure, consisting of 24 variants according to the K–S OR, is shown in Fig. 8b, f, where the PAG with the highest Schmid factor for {110} < 111 > slip system is outlined by black dashed lines. For the two samples, the ideal K–S OR is compared with the experimentally determined OR for the PAG having the highest Schmid factor, as it is the grain that is favorably oriented for slip. The ideal ORs of the partially crept AR sample and uncrept RT sample are displayed as points in their (001) pole figures, which are displayed in Fig. 8c, g. The corresponding experimental ORs are shown in Fig. 8d, h. For reference, the {100}, {110}, and {111} pole figure maps of the two samples are shown in Fig. 8i, j, respectively, and the maximum MUDs of both samples are listed in Table 2. The deviations of the measured ORs in the partially crept AR sample are considerably different from the ideal KS ORs (see Fig. S11), indicating that there is significant sub-grain reorientation after creep. The pronounced texture intensity along the easy glide < 111 > direction with the MUD of 8.27 (see Fig. 8i), in the pole figures of the partially crept AR sample further reinforces this observation. In addition, sharpening of the crystallographic texture along the < 111 > direction influences slip activity and consequently enhances creep deformation. In contrast, the ORs of the uncrept RT sample match well with that of the ideal KS. Moreover, the uncrept RT sample has a maximum MUD of 2.3, which is significantly lower than that of the partially crept AR sample but slightly higher than that of the uncrept AR sample (see Table 2). Regardless, the texture of the uncrept RT sample is relatively random. This suggests that the change in lattice orientation from the ideal K–S relationship, which occurs in the partially crept AR sample during creep (see Fig. S11), is partially reversed when it is subjected to the RT treatment. In contrast, with the exception of maximum MUD, the microstructural features and sub-grain orientations of the uncrept RT sample are similar to that of the uncrept RTUD sample (see Table 2).

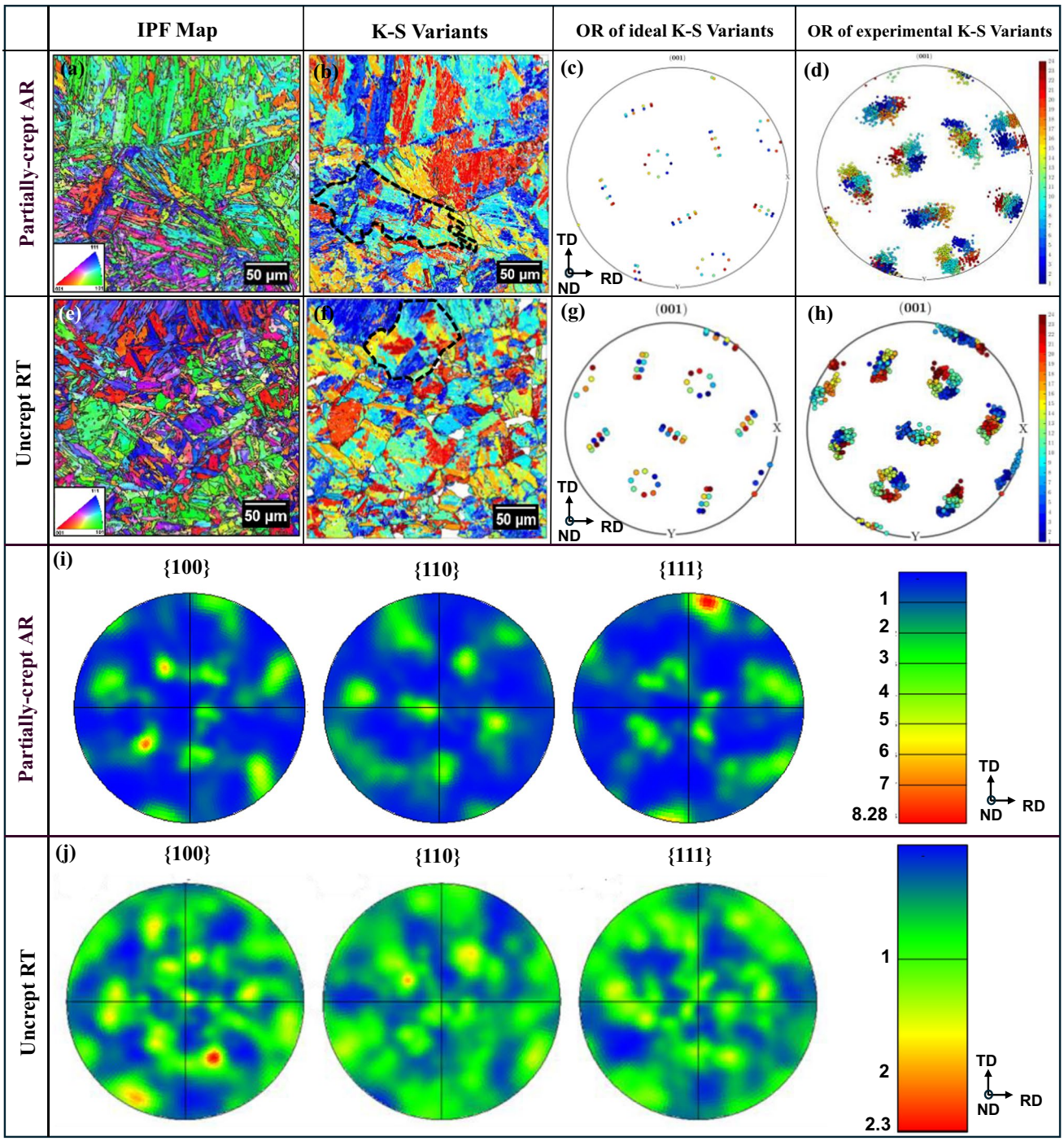


Figure 8 IPF maps of **a** partially crept AR and **e** uncrept RT samples. The corresponding martensitic block variants, based on the K–S OR, are displayed in **b** and **f**, respectively. **c** and **d** The ORs of the ideal and experimental K–S variants of the partially crept AR and **g** and **h** uncrept RT samples, respectively. {100}, {110}, and {111} pole figures with texture intensity for **i** partially crept AR and **j** uncrept RT sample.

Overall, it is evident that during the creep of the AR sample, lath and $M_{23}C_6$ precipitates undergo coarsening, the lath/sub-grains reorient themselves along the easy slip direction and Laves phases form at sub-grain boundaries. RT treatment refines the lath/sub-grains, reduces the area fraction and size of $M_{23}C_6$ precipitates, dissolves the Laves phases, reorients the lath/sub-grains to the ideal K–S OR, and introduces more

distortion in the lath/sub-grains. Also, the microstructural features of the sample after RT treatment are similar to those of the RTUD sample.

Microstructure of creep-ruptured AR and RT samples

From the creep-ruptured AR and RT samples, small pieces are extracted at locations away from the creep-fractured region**.** The microstructures of the creep-ruptured AR and RT samples are shown in Fig. 9a, b, respectively. Their corresponding higher magnification images are shown in Fig. 9c, d, respectively. A_{M23C6} precipitates in the creep-ruptured AR and RT samples are measured and listed in Table 2. In both the creep-ruptured AR and RT samples, A_{M23C6} is 9%.

TEM images of the creep-ruptured AR and RT samples are shown in Fig. 10. L and δ_{M23C6}, $\delta_{MX,}$ c/a ratios, and ρ of the two samples are measured and listed in Table 2. In the creep-ruptured AR sample (see Fig. 10a), L is ~ 959 ± 85 nm, which is 42% coarser than that in the uncrept AR sample. Additionally, d_{M23C6} is 234 ± 21 nm and δ_{M23C6} is 421 ± 76 nm, which is 1.4 times coarser and 43% higher than that in the uncrept AR sample, respectively. d_{MX}, A_{MX}, and δ_{MX} of creep-ruptured AR sample are 32 ± 4 nm, 0.5%, and 151 ± 38 nm, respectively, which is similar to the uncrept AR sample. L in the creep-ruptured RT sample is 998 ± 78 nm (see Fig. 10e), which is similar to that of the creep-ruptured AR sample and almost twice of that of the uncrept RT sample. Moreover, d_{M23C6} and δ_{M23C6} in the creep-ruptured RT sample are 170 ± 14 nm and 306 ± 50 nm, respectively, which is 1.5 times higher and 15% higher than that of the uncrept RT sample, respectively. Interestingly, ultrafine spherical V and Nb-rich MX carbonitrides [33] are observed within the laths of the creep-ruptured RT sample (see Fig. 10g), which is not observed in the creep-ruptured AR sample. d_{MX}, A_{MX}, and δ_{MX} of the creep-ruptured RT sample are 18 ± 4 nm, 0.7%, and 76 ± 34 nm, respectively. Note that d_{MX} and δ_{MX} of the creep-ruptured RT sample are 25% and 33% lower than those in the uncrept RT sample (see Table 2). However, there is a slight increase in A_{MX} of the creep-ruptured RT sample, compared to that in other samples.

In Fig. 10b, f, tangled dislocations are observed near these MX precipitates, which indicates that dislocations interact with them. The c/a ratio of laths of creep-ruptured AR and RT samples is 1 in both cases,

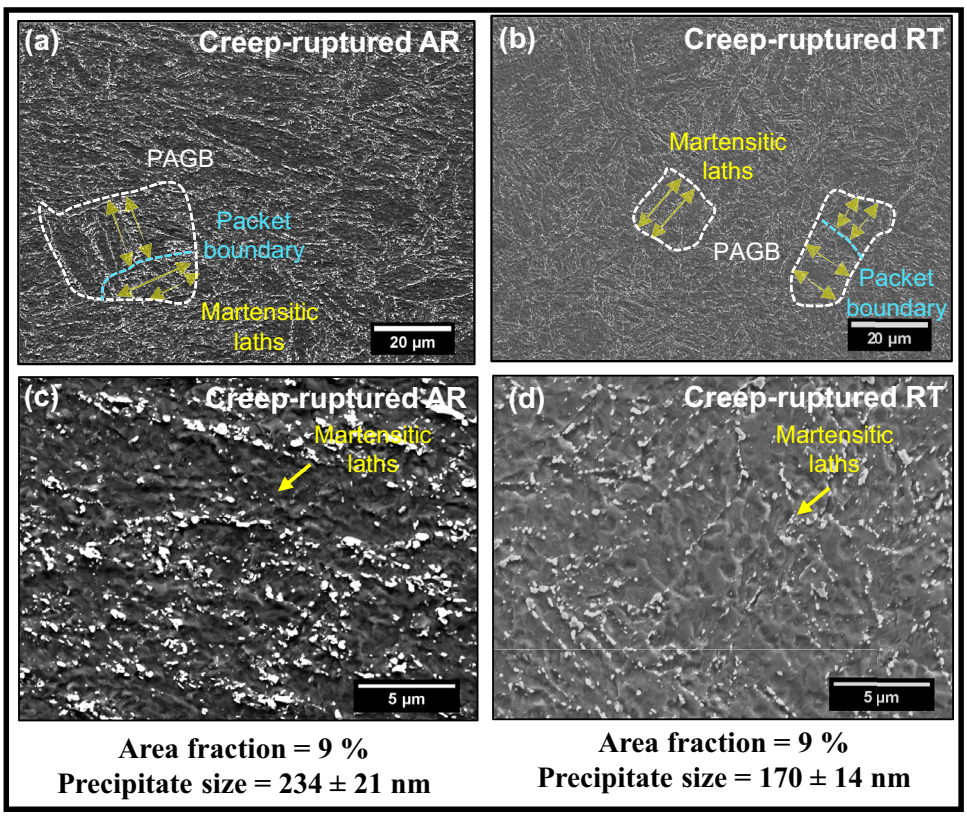


Figure 9 Microstructures of **a** and **c** creep-ruptured AR, **b** and **d** creep-ruptured RT samples.

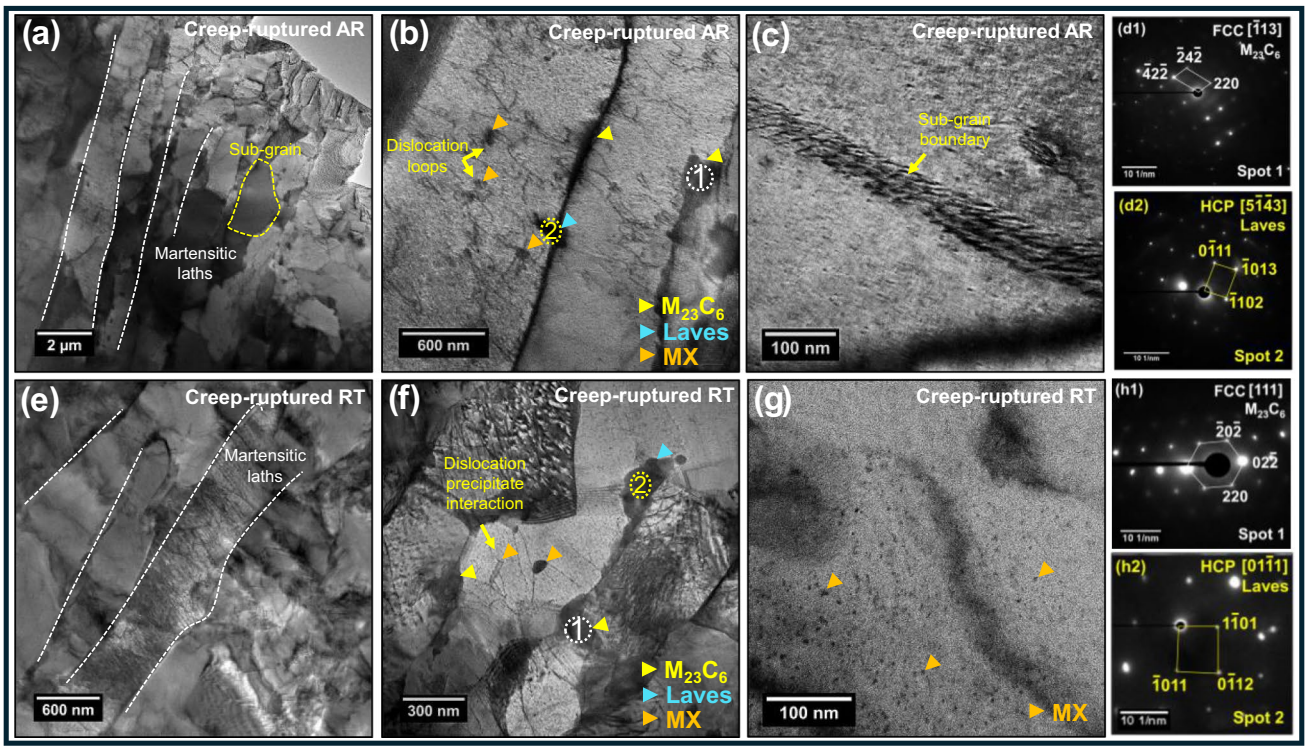


Figure 10 **a**–**c** Bright-field TEM images of the creep-ruptured AR sample and **d1** and **d2** SAED patterns from spots 1 and 2 labeled in **b**. Bright-field TEM images **e**–**g** of creep-ruptured RT sample and **h** SAED patterns from spot 1 and 2 labeled in **f**.

and their ρ is 0.95×10^{14} and 0.98×10^{14}, respectively. The corresponding c/a ratios and ρ of their uncrept counterparts are higher (see Table 2), which indicates that the distortion of the laths and the defect density in them reduce during creep. Finally, Laves phases are observed in both samples (see Fig. 10b, f).

Next, the changes in the orientations of laths in creep-ruptured AR and RT samples are analyzed. The IPF map, pole figure maps, and the positions of the 24 K–S variants for both samples are shown in Fig. 11. The PAG with the highest Schmid factor in creep-ruptured AR and RT samples for the $\{110\}<111>$ slip system is outlined with white dashed lines in Fig. 11b, f, respectively. The pole figures containing ideal and experimentally measured ORs of the PAG in the creep-ruptured AR sample are shown in Fig. 11c, d, respectively. For the creep-ruptured AR sample, the deviation from the ideal K–S OR is significant, which suggests that its laths undergo substantial lattice reorientation during creep (see Fig. 11c, d). This reorientation toward easy glide is further confirmed from pole figures (see Fig. 11i, j), where a strong (111) pole intensity, with a maximum MUD of 11.5, is observed in the creep-ruptured AR sample. However, in the creep-ruptured RT sample, the extent of deviation of the experimental OR from the ideal OR is considerably lower (see Fig. 11g, h). This inference is further reinforced by the fact that the texture of the creep-ruptured RT sample remains largely random as the maximum MUD is only 2.4 (see Fig. 11j). This indicates that while the laths in the AR sample tend to reorient themselves along the easy glide direction and also deviate significantly from near K–S OR, this reorientation does not occur in the RT sample to a significant extent, as the texture remains random, and the block width remains nearly unchanged during creep exposure.

Overall, during creep, lath sub-grains significantly coarsen to ~ 900–1000 nm and the area fractions of $M_{23}C_6$ increase to 9% in both samples. Similarly, the ρ and the matrix distortion in both samples are similar after creep. However, there are some significant microstructural differences in both samples, which are as follows. The size of $M_{23}C_6$ and their interparticle spacing increases considerably. Moreover, a higher fraction of laths reorients along the easy glide direction during creep in the creep-ruptured AR sample compared to that in the creep-ruptured

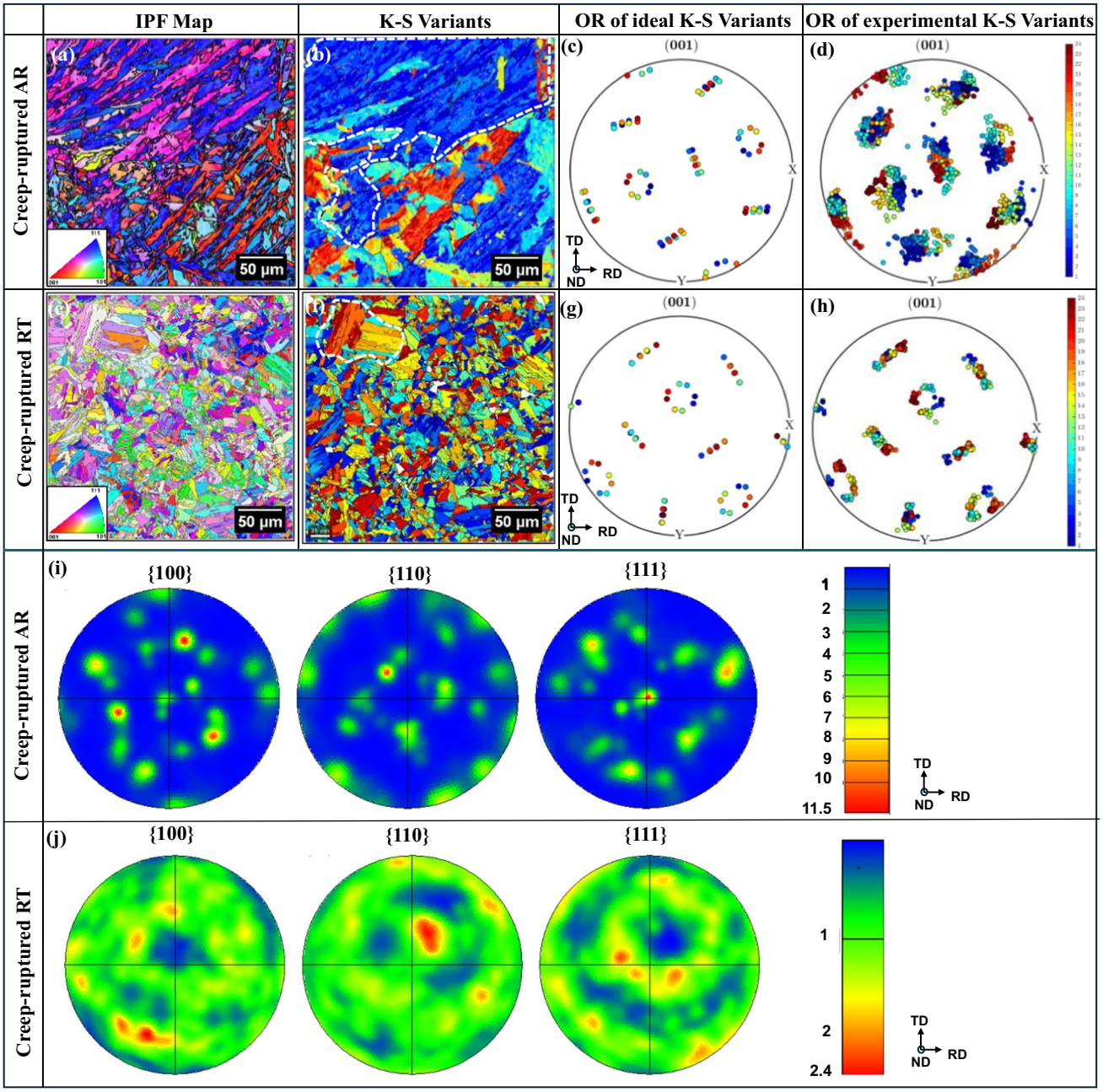


Figure 11 IPF maps of creep-ruptured **a** AR and **e** RT samples. The corresponding martensitic block variants, based on the K–S OR, are displayed in **b** and **f**, respectively. **c** and **d** The ORs of the ideal and experimental K–S variants of creep-ruptured **g** AR and **h** RT samples, respectively. {100}, {110}, and {111} pole figures with texture intensity for creep-ruptured **i** AR and **j** RT sample.

RT sample. Additionally, the size and interparticle spacing of MX precipitates decreases in creep-ruptured RT sample, although its area fraction slightly increases, compared to that in both uncrept RT and creep-ruptured AR samples.

Fracture surface morphology

Figure 12 shows the fracture surfaces of creep-ruptured AR and RT samples. The fracture surface contains several dimples and craters, which are characteristic of transgranular failure and creep cavitation,

respectively. Moreover, within these craters, nanometer-sized precipitates are visible, which suggests that cavities form in the vicinity of precipitates. The precipitates inside these cavities are mostly Laves phases [13]. While there are several small cavities in the creep-ruptured RT sample, those in the creep-ruptured AR sample are fewer in number but larger in size.

Discussions

Microstructure evolution of P91 steel after heat treatments

When P91 steel is first heated at 1050 °C for 6 h, it undergoes complete transformation to austenite. On oil quenching, martensite laths, which have a body-centered tetragonal (BCT) structure, form within the parent austenite grains. These martensite laths have the body-centered tetragonal (BCT) structure and share the K–S OR with the parent austenite grain. During tempering at 750 °C for 15 h, carbon atoms diffuse out of martensite and react with chromium, niobium, molybdenum, and vanadium to form $M_{23}C_6$- and MX-type precipitates. This diffusion process relaxes the distortion in the martensite structure and transforms the crystal structure to the body-centered cubic (BCC) structure [5]. Additionally, tempering leads to the migration of lath boundaries, which leads to lath coarsening without compromising the near K–S OR with the parent austenite grains [4]. In addition, owing to the OR between laths and the parent austenite grains, the former inherits the random texture of the latter, which explains the lack of a preferred orientation in the pole figures of the uncrept AR sample shown in Fig. 2e.

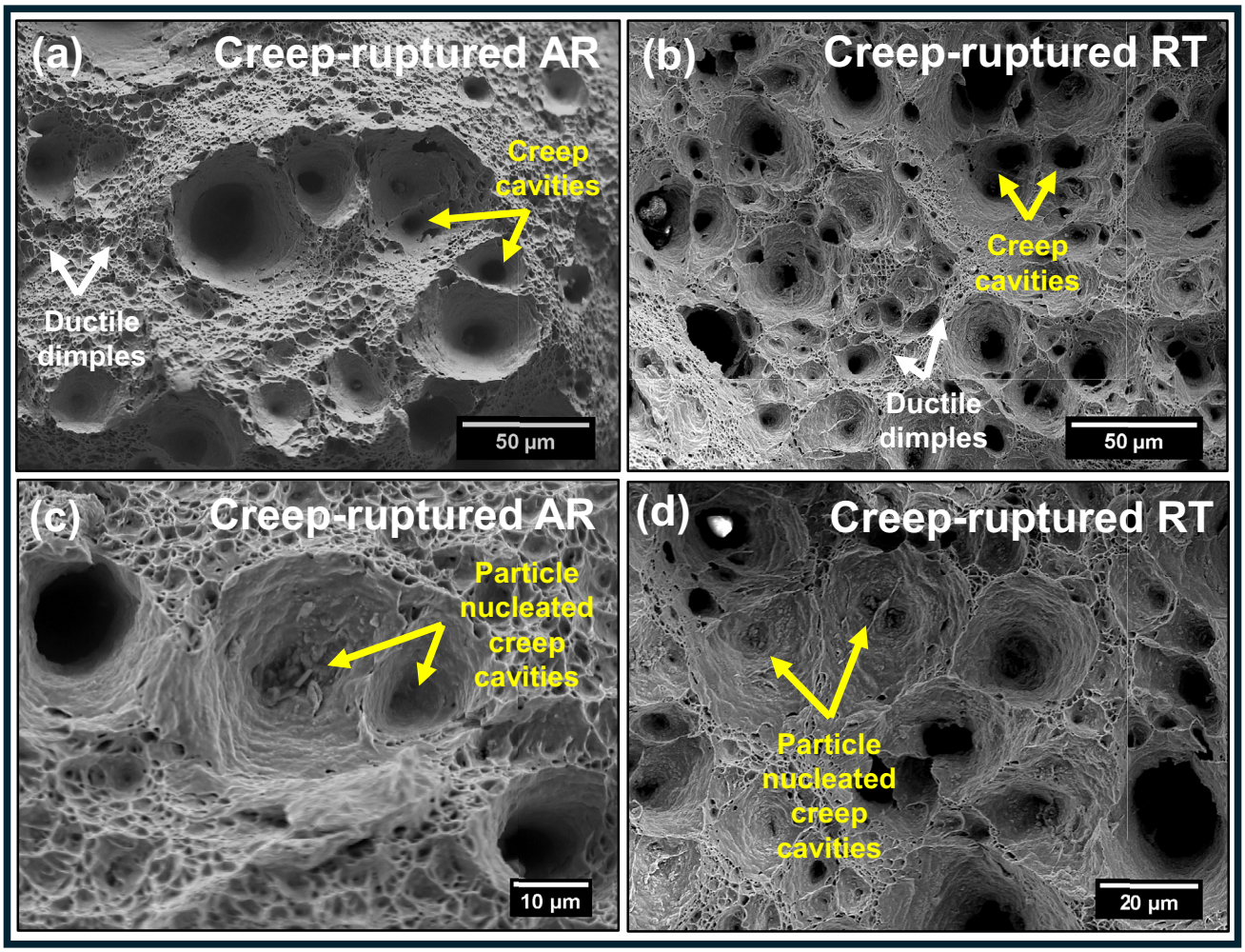


Figure 12 Fracture surface morphology of creep-ruptured **a**, **c** AR and **b**, **d** RT samples.

On performing the re-normalizing treatment at 1050 °C for 2 h followed by re-tempering for 2 h on the uncrept AR sample, which is referred to as the uncrept RTUD sample (see Fig. 1), there are several microstructural changes, which are mentioned in our previous study [11] and are as follows. The re-normalizing treatment dissolves all the $M_{23}C_6$ carbides and re-transforms the martensite to austenite. Although the absence of $M_{23}C_6$, which plays an active role in pinning grain boundaries, would facilitate the growth of these austenite grains during re-normalizing, the shorter duration of the treatment (~ 2 h) ensures limited austenite grain growth. The marginal increase in the PAG size in the uncrept RTUD sample, compared to that of the uncrept AR sample, is attributed to this effect (see Fig. S1). In contrast, MX precipitates, which possess higher thermal stability at 1050 °C, only partially dissolve during normalizing [34–36]. The slight reduction in d_{MX} of the uncrept RTUD sample without much change in A_{MX}, compared to that in the uncrept AR sample, supports this inference (see Table 2). On cooling, carbon-rich martensite laths reform and maintain the near K–S OR with their parent austenite grain. During the subsequent short-term tempering treatment (~ 2 h), carbon again diffuses out from the martensite, which leads to re-coarsening of the martensitic lath and the reprecipitation of $M_{23}C_6$- and MX-type precipitates. However, the extent of lath sub-grain re-coarsening and reprecipitation is limited, owing to the relatively short tempering treatment duration of 2 h, as opposed to that performed for the uncrept AR sample, which is 15 h. This explains the comparatively lower L, d_{M23C6}, and A_{M23C6} in the uncrept RTUD sample than those in the uncrept AR samples (see Table 2). Moreover, owing to higher carbon retention within martensite laths in the uncrept RTUD sample, it is expected to be more distorted, which indeed reflects in higher ρ and c/a compared to that of the uncrept AR sample (see Table 2). In addition, owing to shorter tempering time, there is limited Oswald ripening of the $M_{23}C_6$- and MX-type precipitates, which implies that the average distance between these precipitates is expected to be lower in the uncrept RTUD sample than that in the uncrept AR sample, which is indeed observed (see Table 2).

Creep mechanisms and microstructural evolution during creep

In our previous study [11], it was determined that the duration of the primary stage of creep is negligible compared to that of the steady-state creep. Moreover, the effective stress exponent, n_{eff}, for P91 steel is in the range of 4.5–5.5, which implies that climb-assisted dislocation annihilation at the lath sub-grain boundaries is the governing creep mechanism in the steady-state creep regime [14, 37]. This implies that the steady-state creep rate or $\dot{\varepsilon}_{min}$ is determined by the balance between the rate of dislocation climb-mediated relaxation and the rates of strengthening processes, which retard dislocation and lath sub-grain boundary motion [11].

Dislocation climb-mediated relaxation involves two simultaneous processes. First, dislocations move from the lath interior toward the lath sub-grain boundary via climb and glide. Second, dislocations present at the sub-grain boundaries and those that migrated from the lath sub-grain interior climb along the lath sub-grain boundaries and annihilate when they encounter opposing dislocations. During the process of annihilation, the lath sub-grain boundaries undergo migration, which leads to the growth of the lath sub-grains [11, 38]. One possible mechanism of lath coarsening, proposed by Abe [7], involves dislocation climb and annihilation-induced migration of a Y junction that connect two converging sub-grain boundaries. These processes lead to reduction in dislocation density within the lath sub-grains, which is indeed observed in the partially crept and creep-ruptured AR sample compared to that in the uncrept AR sample (see Table 2). Similarly, the latter process also explains the larger L of partially crept and creep-ruptured AR sample than that of the uncrept AR sample (see Table 2). Note that in the present analysis, dislocation density is used as a simplified metric to represent the evolving dislocation structure during creep. However, it is recognized that dislocation character and their spatial distribution can also influence the interface-controlled kinetics, as reported in recent studies [39, 40]. Furthermore, although deformation twinning may act as a secondary accommodation mechanism under high local stress concentrations near lath or packet boundaries [41], it is generally suppressed in tempered martensitic steels at elevated temperatures due to the high stacking fault energy of the BCC ferritic matrix. Consistent with this, no evidence of deformation twins was observed in the present study, indicating that creep deformation is primarily governed by dislocation mediated processes.

In addition, the increase in < 111 > texture intensity of partially crept and creep-ruptured AR samples

compared to that of the uncrept AR sample is also attributed to the lath coarsening phenomenon (see Figs. 8, 11). Note that dislocation climb and glide preferably occur in laths that have the highest Schmid factor, as they are favorably oriented for slip. Since laths with the < 111 > orientation have the highest Schmid factor, their boundaries preferentially migrate, leading to their coarsening at the expense of laths with other orientations. Consequently, there is an increase in the number of lath with the < 111 > orientation, which manifests as an increase in the MUD of the < 111 > texture of the partially crept and creep-ruptured AR sample (see Fig. 8) than that of the uncrept AR sample. Owing to the increased fraction of < 111 > lath sub-grains, the OR between the laths and the parent austenite grain will also change. This explains the observed deviation of the OR of laths in the partially crept and creep-ruptured AR sample from the ideal K–S relationship (see Fig. 11). Note that such deviations from the ideal K–S OR may alter the crystallographic character and misorientation of martensitic intervarient boundaries. Previous studies [4, 24, 42] have shown that the orientation and plane character of these interfaces can influence dislocation transmission across boundaries and thereby affect the plastic deformation behavior. In BCC martensite, where {110} planes represent the primary slip planes, the relative alignment between these slip systems and the interface plane can modify the interaction between dislocations and martensitic boundaries. However, in the context of high-temperature creep deformation, the direct influence of deviations from the ideal K–S OR on boundary mobility and creep kinetics is not yet fully established and may require a dedicated investigation. The present observations, therefore, primarily provide a crystallographic description of the interface structure.

Alternately, these relaxation processes are countered by the following strengthening processes. First, the dissolved interstitial carbon in the lath sub-grains hinder the motion of dislocations via the solute drag effect [43, 44]. This implies that laths that have higher carbon content are more effective in mitigating dislocation mobility. Second, MX precipitates inside the lath can restrict the motion of dislocations to the grain boundaries. Interactions between dislocations and MX precipitates are indeed observed in the partially crept and creep-ruptured AR samples (see Figs. 7, 10), which supports this conjecture. Third, $M_{23}C_6$ carbides at the lath sub-grain boundaries are obstacles for dislocation climb, which can hinder their annihilation with their opposing pairs [15]. This implies that the mean free path for dislocation climb corresponds to δ_{M23C6}, which in turn means that lesser spacing between $M_{23}C_6$ precipitates can more effectively hinder dislocation climb. Fourth, the $M_{23}C_6$ precipitates apply Zener pressure on the lath sub-grain boundaries and prevent their motion [35]. Note that the extent of Zener pressure also scales with δ_{M23C6} as it can act over a larger length of the lath sub-grain boundary.

Note that with increasing duration of creep, the rate of each of these strengthening processes diminishes, which accelerates the rate of creep relaxation processes, which in turn, leads to the onset of the tertiary or acceleration regime of creep. A brief summary of the reasons leading to the decrease in the rate of each strengthening process is as follows. First, the solute drag effect diminishes over time as the carbon diffuses out of the martensite during creep. An estimate of the dissolved carbon in martensite is obtained from the measured c/a ratio [45]. Figure S10 shows the variations of dissolved carbon for different c/a ratios of martensite. From this plot, the wt.% of dissolved carbon in uncrept AR sample, partially crept AR sample, and creep-ruptured AR sample is 0.05, 0.01, and 0.01, respectively, which suggests that carbon diffuses out from the martensite lath during creep. Second, the MX and $M_{23}C_6$ precipitates coarsen due to Oswald ripening and the outward diffusion of interstitial carbon, which would lead to an increase in their sizes and their interparticle spacing. The higher d_{M23C6}, δ_{M23C6} d_{MX}, and δ_{MX} in the partially crept and creep-ruptured AR samples compared to that in its uncrept counterpart are an outcome of this effect (see Table 2). Owing to the increase in the interparticle spacing, the effectiveness of MX and $M_{23}C_6$ in hindering dislocation motion through the lath and climb along the lath sub-grain boundaries diminishes over time. Similarly, the increased interparticle spacing of the $M_{23}C_6$ precipitates at the lath sub-grain boundary also diminishes the Zener pressure applied by the former and hastens lath sub-grain coarsening. Note that lath sub-grain coarsening during creep deformation leads to microstructural instability, which in turn triggers the onset of the tertiary creep regime and eventually creep rupture [15].

In our previous work, it was noted that short-term normalizing followed by a tempering treatment performed on the AR sample—the same performed to

obtain RTUD sample in this study—enhances its creep life significantly at different stresses and temperatures [11]. Indeed, this enhancement in creep life of the RTUD sample is illustrated in the LMP plots shown in Fig. 5. We attributed the enhanced creep life of the RTUD sample to its relatively lower initial L and δ_{M23C6} (see Table 2) compared to that of the AR sample [11]. The rationale for this assertion is that the sample with smaller L would take significantly longer time to coarsen and trigger microstructural instability than that with larger L. Moreover, lower δ_{M23C6} ensures that the Zener pinning force on the lath sub-grain boundaries of the RTUD sample will be significantly higher than that in the AR sample. Conversely, when $M_{23}C_6$ precipitates undergo Oswald ripening, where larger precipitates grow at the expense of smaller ones, δ_{M23C6} decreases, and the pinning pressure on the lath sub-grain boundary decreases.

It is noteworthy that the creep life of the RT sample, which corresponds to the partially crept AR sample that is subjected to the same above-mentioned short-term normalizing and tempering treatment, is the same as that of the RTUD sample (see Fig. 1). This implies that the short-term normalizing and tempering treatment largely restores the creep damage and deformation history of the partially crept AR sample. In fact, the good match between the microstructural features of the RT sample, such as d_{M23C6}, δ_{M23C6}, d_{MX}, and $\delta_{MX,}$ matches with those of the RTUD sample (see Figs. 6, 7, 8 and S1, and Table 2), suggesting that microstructural tailoring of P91 via the applied heat treatments is independent of the creep damage in the material. Furthermore, the long-term stability of the rejuvenated microstructure can be inferred from the stress-LMP relationship (Fig. 5), where the creep rupture life of the RT sample closely matches with that of the RTUD condition, indicating that the long-term creep performance of the RT sample is believed to be comparable to that of the RTUD samples.

Lath coarsening kinetics

To further quantitatively assess the evolution of L and δ_{M23C6} during creep of P91 sample, the continuum damage mechanics (CDM) model, developed by Xiao et. al. [12], is utilized. In this model, the coarsening kinetics of tempered martensitic laths during creep are modeled using a dislocation-based approach that incorporates Zener drag and boundary mobility, where the rate of lath coarsening, $\dot{L}$, is

$$\dot{L} = M_b \left[P_b - 2\pi \left(\sum_{i=1}^{n} r_i^2 N_i \right) \gamma_b \right] \tag{3}$$

where M_b is the mobility of lath boundary dislocations and γ_b is the surface energy of the lath boundary. The Zener drag term accounts for the pinning effect from the precipitates, with r_i and N_i representing the average radius and number density of precipitates. P_b is the pressure on the lath/sub-grain boundary, which is calculated from [12],

$$P_b = 4Gb^2\rho/3. \tag{4}$$

The coarsening behavior of $M_{23}C_6$ and MX carbides follows the Lifshitz–Slyozov–Wagner (LSW) model, where [12],

$$d_t^m - d_o^m = k_d t \tag{5}$$

where d_t and d_o are the average precipitate diameters at time t and before creep, respectively, and m is the growth exponent, which depends on the diffusion mechanism. Note that $m \sim 3$ for $M_{23}C_6$ as it undergoes lattice diffusion-controlled growth and for MX $m \sim 5$ as it undergoes dislocation pipe diffusion-controlled growth [12]. Table 4 lists the parameters used to estimate the variations of L with increasing creep duration in AR and RT samples. The boundary mobility, M_b, is estimated from Eq. (3) via an iterative process, which ensures that the obtained final L closely matches with that of the experimentally observed value. The estimated M_b values for AR and RT samples are 4.5×10^{-20} and 2.5×10^{-20} m^4/Js. The lower mobility in RT sample is attributed to the refined, more stable microstructure produced by the rejuvenation treatment, which enhances precipitate-induced boundary pinning and thereby reduces the mobility of the boundaries. A Sobol sensitivity analysis evaluated based on [46] indicates that the predicted lath sub-grain growth behavior is primarily governed by boundary mobility and dislocation density, with additional contributions from boundary surface energy and precipitate characteristics through the Zener pinning term (see SI document). Furthermore, although local heterogeneity exists in microstructural parameters such as lath width and precipitate size, the measured variation remains within 10% of the average values (refer to Table 2). Such limited variation is not believed to affect the

Table 4 Parameters used in the CDM model for P91 steel

Parameters	AR	RT
Boundary energy, γ_b, (J/m^2) [10]	1	1
Boundary mobility, M_b (m^4/J.s)	4.5×10^{-20}	2.5×10^{-20}
Precipitate density of $M_{23}C_6$ before creep (m^{-3})	4.87×10^{18}	8.06×10^{18}
Precipitate density of MX before creep (m^{-3})	8.84×10^{19}	2.24×10^{20}
Climb velocity (m/s) [12]	1×10^{-12}	1×10^{-12}

CDM model predications based on spatially averaged parameters. Also, note that during creep deformation, precipitate coarsening and boundary migration are coupled processes. In some local regions, excessive precipitate coarsening may reduce the pinning effectiveness, allowing the lath sub-grain boundary to migrate while leaving precipitates stranded within the lath sub-grain interior, as occasionally observed in our previous study [11]. However, in most cases, precipitate coarsening occurs synergistically with boundary migration, with precipitates remaining attached to the boundaries. Limited redistribution of precipitates along migrating boundaries may therefore occur, although coarsening of existing boundary precipitates remains the dominant observation.

It is worth noting that owing to its low volume fraction (~ 0.2%) and relatively large interparticle spacing, the Zener pinning pressure from Laves phase is negligible compared to fine MX precipitates and therefore does not significantly contribute to lath/sub-grain boundary pinning. However, this does not imply that Laves phase is insignificant in creep damage evolution. Laves particles act as preferential sites for cavity nucleation and can strongly influence tertiary creep and creep failure initiation (see Fig. 12). Thus, while their role in boundary pinning is minimal, their contribution to tertiary creep damage remains important.

Figure 13 shows the variations of L and d_{M23C6} precipitates as a function of time. Note that L of both AR and RT samples increases with time. However, the rate of increase in L is higher for the AR sample compared to that of the RT sample. For instance, L increases from 676 ± 54 nm to 959 ± 85 nm in 992 h in the AR sample but the same increase in L in the RT sample takes 3800 h. It is evident that the coarsening rate of lath sub-grains is inversely correlated with initial L. Similarly, although d_{M23C6} also increases in both AR and RT samples, the rate of increase in d_{M23C6} is higher in the former than that in the latter. From these plots, L in the steady-state creep regime of AR and RT samples, L_{ss}^{AR} and L_{ss}^{RT} are marked with blue dashed regions. From

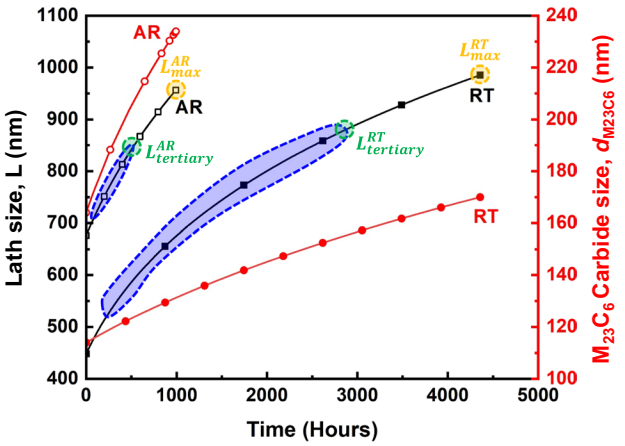


Figure 13 Calculated variations of lath/sub-grain width and $M_{23}C_6$ carbides during creep exposure.

this, the ratios of the steady-state L of AR and RT samples, $\frac{L_{ss}^{AR}}{L_{ss}^{RT}}$, and ratios of their steady-state creep rates, $\frac{\dot{\varepsilon}_{min}^{AR}}{\dot{\varepsilon}_{min}^{RT}}$, are related via the power-law relationship [12, 47],

$$\frac{\dot{\varepsilon}_{min}^{AR}}{\dot{\varepsilon}_{min}^{RT}} = \left(\frac{L_{ss}^{AR}}{L_{ss}^{RT}}\right)^{n} \quad (6)$$

Substituting the values from Fig. 13 and Table 2, n is ~ 5.3. However, note that n is not a constant and is expected to be sensitive to temperature and creep stress.

In Fig. 13, L at creep rupture for AR and RT samples, L_{max}, which are 959 ± 85 nm and 998 ± 78 nm (see Table 2) respectively, is indicated using orange dashed circles. Note that creep failure generally occurs when the lath sub-grain width exceeds ~ 900–1000 nm, as also observed for samples tested under different stresses and temperatures in our previous work (refer to Table S5). Also, L at the onset of tertiary creep for both AR and RT samples, $L_{tertiary}$, are encircled by green dashed circles. For both samples, $L_{tertiary}/L_{max}$ is 0.89. Similarly, $L_{tertiary}/L_{max}$ for AR, RT, and RTUD

samples that are creep-tested at different temperatures and stresses are calculated and listed in Table S2. In all cases, note that $L_{tertiary}/L_{max}$ ~ is 0.89, which suggests that 89% of the lath coarsening occurs before the onset of the tertiary regime of creep, whereas the rest of the 11% occurs in the tertiary regime of creep.

Implications of creep life rejuvenation and other considerations

The main highlight of this study is the observation that while the short-term normalizing and tempering treatment does not alter quasi-static mechanical properties such as strength and ductility (see Fig. 3), it largely restores the creep history of P91 steel and even appears to enhance its creep life by several folds. This implies that the above-mentioned heat treatment can be integrated with routine maintenance protocols in industry and applied on P91 components exposed to high-temperature service to extend their life significantly (assuming that creep is the primary concern in such components). It is then worth asking whether the routine application of this heat treatment strategy can extend the creep lives of P91 components indefinitely. The answer to this question is not straightforward and requires more careful consideration of the service conditions and safety. Note that we apply the short-term heat treatment when the AR sample has reached 50% of its overall creep life, t_r, which is close to the onset of the tertiary creep regime ($0.56t_r$). Therefore, we believe that if the material has not undergone creep in the tertiary regime, the rejuvenation treatment will be highly effective. This is because the deformation mechanisms in the tertiary regime of creep are unknown and may involve processes such as void nucleation, which can lead to permanent damage in the material. However, it is not clear whether the rejuvenation treatment would work on a component that is undergoing creep in the tertiary regime, and it is a topic of future research.

In the context of the current study, one way to assess the stage of creep deformation in the component is to design a sacrificial appendage in the relevant component that experiences the same service conditions as the main component and then routinely cut a piece from it during service to assess its microstructure. Provided $L_{tertiary}/L_{max}$ is < 0.89 in this sacrificial piece, the component has undergone steady-state creep and can be rejuvenated using the short-term normalizing and tempering heat treatment. However, note that while this treatment erases creep damage, it does not recover the permanent change in the dimensions of the component that occurs during creep. Given that design of power plant components is usually conservative and requires strict adherence to factors of safety, performing the rejuvenation heat treatment on a component that has undergone uniform but significant creep deformation may not serve any purpose as the component would have to be replaced. In such a case, the designer has to specify the maximum creep strain that can be accommodated in the component, if one were to consider the rejuvenation approach. Regardless, it is worth examining in future studies whether the rejuvenation effect of the prescribed short-term heat treatment will be as effective in each iteration when performed multiple times on a component undergoing creep.

On a related note, the dramatic increase in creep resistance of the RTUD and RT samples is attributed to the significant reduction in L compared to that in the AR sample. This is an outcome of the relatively short duration (~ 2 h) of the tempering heat treatment performed on the AR sample after normalizing, which does not allow the lath sub-grains to coarsen significantly. In this context, it appears that the growth of lath sub-grains could be further curtailed by performing tempering treatments for even shorter durations. However, on the other extreme, performing tempering is essential for relieving strains that develop from the austenite to martensite transformation. Therefore, optimizing the duration of tempering treatment to maximize creep life and minimize distortion is a topic for future study.

Note that in other materials such as Ni-based superalloys, the extent of creep life rejuvenation by recourse to thermo-mechanical heat treatments is not as effective as that observed in P91 steel [48]. This is attributed to permanent changes in the microstructure of superalloys during creep, such as degeneration of primary MC carbides, which increases the carbon content in the matrix and promotes the coarsening of $M_{23}C_6$ grain boundary carbides, and cannot be reversed by thermo-mechanical treatments. This further highlights the uniqueness of the observed microstructural reversibility in ferritic martensitic steels, which offers a viable opportunity to extend their service life to a significant or near-infinite extent. Also note that the creep rupture results at 600 °C/135 MPa are based on single tests for the AR and RT conditions, together with interrupted specimens at 0.5 t_r. Although repeat creep rupture tests could not be performed owing to

time constraints, the magnitude of the observed creep life enhancement, its agreement with the LMP master curve of RTUD samples, which is estimated from independently tested specimens, and accompanying order of magnitude reduction in minimum creep rate collectively support that the improvement arises from a genuine microstructural reset rather than statistical variability.

While the present results demonstrate the feasibility of creep rejuvenation, practical implementation in large components requires careful engineering assessment. Heating to ~ 1050 °C may introduce risks of distortion, oxidation, surface degradation, and residual stresses, particularly in complex geometries. Moreover, weld metal and heat-affected zones (HAZ), which are often critical in P91 service failure, may respond differently and require independent validation. Any rejuvenation strategy must therefore be integrated with appropriate nondestructive evaluation protocols, including surface damage assessment and hardness monitoring. Therefore, rejuvenation should be viewed as a condition-dependent life extension strategy that requires component-specific validation rather than a universally applicable solution.

Conclusion

In this study, the potential and extent of creep life rejuvenation of P91 steel, which is partially creep-deformed to $0.5t_r$ using a short-term normalizing treatment at 1050 °C for 2 h, followed by tempering at 750 °C for 2 h, is investigated. The key findings of the investigation are as follows:

1. Creep of P91 steel leads to lath sub-grain coarsening from 676 ± 54 nm to 857 ± 64 nm, significant misorientation from the ideal K–S relationship of laths, a change in the MUD of lath orientation from 2.67 to 8.28, and Oswald ripening of $M_{23}C_6$ from 164 ± 18 nm to 188 ± 13 nm at $0.5t_r$. Applying the above-mentioned short-term heat treatment on this partially creep-deformed steel leads to refinement of lath size to 448 ± 41 nm, block reorientation to near K–S relationship, and refinement of $M_{23}C_6$ to 114 ± 15 nm. These microstructural features are similar to those of uncrept steel, which is subjected to the same short-term heat treatment, indicating that the microstructural state is highly reversible and agnostic to creep damage.
2. Room temperature YS and UTS of the as-received steel, which are 509 ± 12 and 644 ± 21 MPa, respectively, do not get significantly altered after the above-mentioned short-term heat treatment. A similar minimal change of 20% and 10% in YS and UTS of the as-received steel after the short-term heat treatment is observed at 600 °C. However, the enhancement in creep life at 600 °C and 135 MPa is almost fourfold after the same heat treatment on the uncrept or partially creep-deformed as-received steel.
3. The primary creep mechanism, which is determined as dislocation climb in previous studies, facilitates lath coarsening via annihilation of opposing dislocations at lath sub-grain boundaries. The MX and $M_{23}C_6$ precipitates retard recovery by hindering the glide and climb of dislocations within lath and lath sub-grain boundaries. The competition between these processes controls lath coarsening kinetics, which is modeled using the continuum damage model. Creep failure occurs when lath sub-grain width exceeds 900–1000 nm.
4. The lath coarsening and precipitate coarsening rates scale with the initial lath and precipitate sizes, respectively, and the steady-state creep rate has a power-law relationship with the steady-state lath width, with an exponent of 5.3. Moreover, 89% of the lath coarsening occurs in the primary and steady-state creep regime, and only 11% occurs in the tertiary creep regime at all stresses and temperatures. This estimate is based on the ratio $L_{tertiary}/L_{max} \approx 0.89$, where $L_{tertiary}$ represents the lath/sub-grain width at the onset of tertiary creep as identified from the creep curve.
5. Rejuvenation treatment can be repeated on the component multiple times during service to extend its creep life, although it cannot recover the creep strain, which implies that component tolerance becomes the limiting step for component replacement in service. The optimization of the short-term heat treatment, which leads to the highest creep life rejuvenation, is unclear and requires further investigations. Finally, the creep life rejuvenation strategy appears to be highly effective in P91 steel, which is not the case in superalloys, where thermo-mechanical treatments on a creep-deformed component only partially enhance their creep life.

Acknowledgements

The authors thank the Central Research Facility (CRF) at IIT Delhi for providing the research facilities used in this study. Financial support from the Prime Minister's Research Fellowship (PMRF) is also appreciated. Furthermore, we appreciate the support and materials provided by the Helmholtz-Zentrum Dresden-Rossendorf (HZDR) Institute in Germany.

Data availability

The datasets used and/or analyzed during the current study are available from the corresponding author on reasonable request.

Declarations

Conflict of interest The authors declare that they have no conflict of interest.

Supplementary Information The online version contains supplementary material available at https://doi.org/10.1007/s10853-026-12714-y.

References

[1] Pandey C, Mahapatra MM, Kumar P, Saini N (2018) Some studies on P91 steel and their weldments. J Alloys Compd 743:332–364. https://doi.org/10.1016/j.jallcom.2018.01.120

[2] Lucacci G (2017) Steels and alloys for turbine blades in ultra-supercritical power plants. Mater Ultra-Supercrit Adv Ultra-Supercrit Power Plants 175-196. https://doi.org/10.1016/B978-0-08-100552-1.00007-5

[3] Zhang K, Shen Z, Li J et al (2026) Anomalous oxidation behavior and enhanced corrosion resistance of a lean-Cr FeCrAl alloy in the oxygenated PWR primary water. Corros Sci 259:113452. https://doi.org/10.1016/j.corsci.2025.113452

[4] Payton EJ, Aghajani A, Otto F et al (2012) On the nature of internal interfaces in a tempered martensite ferritic steel and their evolution during long-term creep. Scr Mater 66:1045–1048. https://doi.org/10.1016/J.SCRIPTAMAT.2012.02.042

[5] Pandey C, Mahapatra MM, Kumar P, Saini N (2018) Some studies on P91 steel and their weldments. J Alloys Compd. 743:332-364. https://doi.org/10.1016/j.jallcom.2018.01.120

[6] Sawada K, Takeda M, Maruyama K et al (1999) Effect of W on recovery of lath structure during creep of high chromium martensitic steels. Mater Sci Eng A 267:19–25. https://doi.org/10.1016/S0921-5093(99)00066-0

[7] Abe F (2004) Coarsening behavior of lath and its effect on creep rates in tempered martensitic 9Cr–W steels. Mater Sci Eng A 387–389:565–569. https://doi.org/10.1016/J.MSEA.2004.01.057

[8] Dudko V, Belyakov A, Kaibyshev R (2017) Evolution of lath substructure and internal stresses in a 9% Cr steel during creep. ISIJ Int 57:540–549. https://doi.org/10.2355/ISIJINTERNATIONAL.ISIJINT-2016-334

[9] Wang Y, Zhou Z, Lu J et al (2026) Effect of Si addition on the oxidation of a 12Cr1Al ODS alloy in liquid LBE. Prog Nucl Energy 193:106226. https://doi.org/10.1016/j.pnucene.2025.106226

[10] Xiao B, Xu L, Zhao L et al (2018) Creep properties, creep deformation behavior, and microstructural evolution of 9Cr-3W-3Co-1CuVNbB martensite ferritic steel. Mater Sci Eng A 711:434–447. https://doi.org/10.1016/J.MSEA.2017.11.061

[11] Parnaik A, Pavan AHV, Das A et al (2024) On enhancing the creep performance of modified 9Cr–1Mo steel by employing a secondary short-term heat treatment. J Mater Sci 59:21494–21514. https://doi.org/10.1007/S10853-024-10439-4/FIGURES/12

[12] Xiao B, Yadav SD, Zhao L et al (2021) Deep insights on the creep behavior and mechanism of a novel G115 steel: micromechanical modeling and experimental validation. Int J Plast 147:103124. https://doi.org/10.1016/J.IJPLAS.2021.103124

[13] Pandey C, Mahapatra MM, Kumar P et al (2017) Microstructure-based assessment of creep rupture behaviour of cast-forged P91 steel. Mater Sci Eng A 695:291–301. https://doi.org/10.1016/J.MSEA.2017.04.037

[14] Shrestha T, Basirat M, Charit I et al (2012) Creep deformation mechanisms in modified 9Cr–1Mo steel. J Nucl Mater 423:110–119. https://doi.org/10.1016/J.JNUCMAT.2012.01.005

[15] Maruyama K, Sawada K, Koike JI (2001) Strengthening mechanisms of creep resistant tempered martensitic steel. ISIJ Int 41:641–653. https://doi.org/10.2355/ISIJINTERNATIONAL.41.641

[16] Maccagno TM, Koul AK, Immarigeon JP et al (1990) Microstructure, creep properties, and rejuvenation of service-exposed alloy 713C turbine blades. Metall Trans A

Phys Metall Mater Sci A 21:3115–3125. https://doi.org/10.1007/BF02647308/METRICS

[17] Lvova E, Norsworthy D (2001) Influence of service-induced microstructural changes on the aging kinetics of rejuvenated Ni-based superalloy gas turbine blades. J Mater Eng Perform 10:299–313. https://doi.org/10.1361/105994901770345015

[18] Koul AK, Castillo R (1988) Assessment of service induced microstructural damage and its rejuvenation in turbine blades. Metall Trans A 19:2049–2066. https://doi.org/10.1007/BF02645208

[19] Zhou Y, Zhang Z, Zhao Z, Zhong Q (2013) Effects of HIP temperature on the microstructural evolution and property restoration of a Ni-based superalloy. J Mater Eng Perform 22:215–222. https://doi.org/10.1007/S11665-012-0246-8

[20] Wang L, Yang XG, Qi HY et al (2021) Microstructural evolution and restoration of creep property for a damaged K403 alloy after rejuvenation heat treatments. Rare Met 40:1865–1871. https://doi.org/10.1007/S12598-020-01434-0/FIGURES/9

[21] Baldan A (1991) Rejuvenation procedures to recover creep properties of nickel-base superalloys by heat treatment and hot isostatic pressing techniques. J Mater Sci 26(13):3409–3421. https://doi.org/10.1007/BF00557126

[22] Panait CG, Zielińska-Lipiec A, Koziel T et al (2010) Evolution of dislocation density, size of subgrains and MX-type precipitates in a P91 steel during creep and during thermal ageing at 600 °C for more than 100,000 h. Mater Sci Eng A 527:4062–4069. https://doi.org/10.1016/J.MSEA.2010.03.010

[23] Nyyssönen T, Gazder AA, Hielscher R, Niessen F (2023) Habit plane determination from reconstructed parent phase orientation maps. Acta Mater 255:119035. https://doi.org/10.1016/J.ACTAMAT.2023.119035

[24] Morito S, Tanaka H, Konishi R et al (2003) The morphology and crystallography of lath martensite in Fe–C alloys. Acta Mater 51:1789–1799. https://doi.org/10.1016/S1359-6454(02)00577-3

[25] Niessen F, Nyyssönen T, Gazder AA, Hielscher R (2022) Parent grain reconstruction from partially or fully transformed microstructures in MTEX. J Appl Crystallogr 55:180–194. https://doi.org/10.1107/S1600576721011560

[26] Fischer T, Zhou T, Dahlberg CFO, Hedström P (2024) Relating stress/strain heterogeneity to lath martensite strength by experiments and dislocation density-based crystal plasticity. Int J Plast 174:103917. https://doi.org/10.1016/J.IJPLAS.2024.103917

[27] Kimura K, Kushima H, Sawada K (2009) Long-term creep deformation property of modified 9Cr–1Mo steel. Mater Sci Eng A 510–511:58–63. https://doi.org/10.1016/J.MSEA.2008.04.095

[28] Parnaik A, Pavan AHV, Silchonok SS et al (2024) High-cycle fatigue behavior of Haynes 282 superalloy subjected to accelerated ageing. Int J Fatigue 182:108234. https://doi.org/10.1016/J.IJFATIGUE.2024.108234

[29] Tamura M, Abe F, Shiba K et al (2013) Larson-miller constant of heat-resistant steel. Metall Mater Trans A Phys Metall Mater Sci 44:2645–2661. https://doi.org/10.1007/S11661-013-1631-0/FIGURES/22

[30] Erami M, Daei-Sorkhabi AH, Vakili-Tahami F (2019) Creep constitutive equations for as-received 9Cr1Mo steel. Int J Press Vessel Pip 176:103947. https://doi.org/10.1016/J.IJPVP.2019.103947

[31] Isik MI, Kostka A, Eggeler G (2014) On the nucleation of Laves phase particles during high-temperature exposure and creep of tempered martensite ferritic steels. Acta Mater 81:230–240. https://doi.org/10.1016/J.ACTAMAT.2014.08.008

[32] Isik MI, Kostka A, Yardley VA et al (2015) The nucleation of Mo-rich Laves phase particles adjacent to M23C6 micrograin boundary carbides in 12% Cr tempered martensite ferritic steels. Acta Mater 90:94–104. https://doi.org/10.1016/J.ACTAMAT.2015.01.027

[33] Xiao B, Xu L, Zhao L et al (2018) Transient creep behavior of a novel tempered martensite ferritic steel G115. Mater Sci Eng A 716:284–295. https://doi.org/10.1016/J.MSEA.2018.01.047

[34] Du Y, Li X, Zhang XU et al (2019) Design and characterization of a heat-resistant ferritic steel strengthened by MX precipitates. Metall Mater Trans A Phys Metall Mater Sci.51:638-647. https://doi.org/10.1007/s11661-019-05525-1

[35] Xu Y, Li W, Wang M et al (2019) Nano-sized MX carbonitrides contribute to the stability of mechanical properties of martensite ferritic steel in the later stages of long-term aging. Acta Mater 175:148–159. https://doi.org/10.1016/J.ACTAMAT.2019.06.012

[36] Panait CG, Zielińska-Lipiec A, Koziel T et al (2010) Evolution of dislocation density, size of subgrains and MX-type precipitates in a P91 steel during creep and during thermal ageing at 600 °C for more than 100,000 h. Mater Sci Eng A 527:4062–4069. https://doi.org/10.1016/J.MSEA.2010.03.010

[37] Zhang XZ, Wu XJ, Liu R et al (2017) Deformation-mechanism-based modeling of creep behavior of modified 9Cr–1Mo steel. Mater Sci Eng A 689:345–352. https://doi.org/10.1016/J.MSEA.2017.02.044

[38] Xu W, Zhang B, Li XY, Lu K (2021) Suppressing atomic diffusion with the Schwarz crystal structure in supersaturated Al–Mg alloys. Science (1979) 373:683–687. https://doi.org/10.1126/science.abh0700

[39] Xu W, Xin YC, Zhang B, Li XY (2022) Stress corrosion cracking resistant nanostructured Al–Mg alloy with low angle grain boundaries. Acta Mater 225:117607. https://doi.org/10.1016/j.actamat.2021.117607

[40] Xu W, Zhang B, Du K et al (2022) Thermally stable nanostructured Al–Mg alloy with relaxed grain boundaries. Acta Mater 226:117640. https://doi.org/10.1016/j.actamat.2022.117640

[41] Huo PD, Huang LK, Song KX et al (2025) High-density metastable annealing twin boundaries-induced extraordinary strain hardening in ultrafine-grained high-entropy alloy. Acta Mater 295:121205. https://doi.org/10.1016/j.actamat.2025.121205

[42] Morsdorf L, Jeannin O, Barbier D et al (2016) Multiple mechanisms of lath martensite plasticity. Acta Mater 121:202–214. https://doi.org/10.1016/J.ACTAMAT.2016.09.006

[43] Hanlumyuang Y, Gordon PA, Neeraj T, Chrzan DC (2010) Interactions between carbon solutes and dislocations in bcc iron. Acta Mater 58:5481–5490. https://doi.org/10.1016/J.ACTAMAT.2010.06.024

[44] Hu SY, Li YL, Zheng YX, Chen LQ (2004) Effect of solutes on dislocation motion—a phase-field simulation. Int J Plast 20:403–425. https://doi.org/10.1016/S0749-6419(03)00094-9

[45] Lu Y, Yu H, Sisson RD (2017) The effect of carbon content on the c/a ratio of as-quenched martensite in Fe–C alloys. Mater Sci Eng A 700:592–597. https://doi.org/10.1016/J.MSEA.2017.05.094

[46] Tian Y, Lu D, Wang W et al (2026) Combining strain-assisted nanoprecipitation with nanotwins to enhance strength of laser additively manufactured high-entropy alloys. Mater Charact 234:116192. https://doi.org/10.1016/j.matchar.2026.116192

[47] Yadav SD, Sonderegger B, Stracey M, Poletti C (2016) Modelling the creep behaviour of tempered martensitic steel based on a hybrid approach. Mater Sci Eng A 662:330–341. https://doi.org/10.1016/J.MSEA.2016.03.071

[48] James A (2001) Review of rejuvenation process for nickel base superalloys. Mater Sci Technol 17:481–486. https://doi.org/10.1179/026708301101510168

Publisher's Note Springer Nature remains neutral with regard to jurisdictional claims in published maps and institutional affiliations.

Springer Nature or its licensor (e.g. a society or other partner) holds exclusive rights to this article under a publishing agreement with the author(s) or other rightsholder(s); author self-archiving of the accepted manuscript version of this article is solely governed by the terms of such publishing agreement and applicable law.